Journal of Nanobiotechnology

RESEARCH

Open Access

Oxygen vacancy-engineered bimetallic nanozymes for disrupting electron transport chain and synergistic multi-enzyme activity to reverse oxaliplatin resistance in colorectal cancer

Dong Zhong[1], Xiaoxin Yang[2*], Jinhui Yang[1], Zhisheng Luo[1], Zhichao Feng[3], Mengtian Ma[4], Yunjie Liao[5], Yongxiang Tang[1], Yu Wen[6], Jun Liu[2*] and Shuo Hu[1,7,8*]

Abstract

In colorectal cancer treatment, chemotherapeutic agents induce reactive oxygen species (ROS) production, which promotes NAD^+ accumulation in tumor cells, reducing treatment sensitivity and worsening patient prognosis. Targeted depletion of NAD^+ presents a promising strategy to overcome tumor resistance and improve patient prognosis. Here, we designed a dual-metallic nanozyme ($CuMnO_{x-V}$@Oxa@SP) with defect engineering, modified by soy phospholipids (SP) and loaded with oxaliplatin (Oxa). This nanozyme uses its oxygen-deficient active sites to rapidly and irreversibly degrade NAD^+ and NADH into nicotinamide and ADP-ribose derivatives, disrupting the electron transport chain (ETC) and compromising tumor antioxidant defenses. It also inhibits the glutathione S-transferase P1 (GSTP1) pathway, weakening tumor detoxification and enhancing chemotherapy sensitivity. Density functional theory calculations revealed that the synergistic effect among multi-enzyme active centers endows the $CuMnO_{x-V}$ nanozymes with excellent catalytic activity. In the tumor microenvironment (TME), $CuMnO_{x-V}$ nanozymes exhibit peroxidase, oxidase, and NAD^+ oxidase-mimicking activities. $CuMnO_{x-V}$ generates multiple ROS and depletes NAD^+ while preventing their regeneration thereby triggering a cascade amplification of oxidative stress. This, coupled with targeted chemotherapy drug delivery, restores chemosensitivity in refractory tumors and exposes the vulnerabilities of resistant colorectal cancer cells to ROS.

Keywords ETC disruption, Bimetallic nanozymes, NAD^+ depletion, Multi-enzyme activity, Oxaliplatin resistance

*Correspondence:
Xiaoxin Yang
yxxawy@163.com
Jun Liu
junliu123@csu.edu.cn
Shuo Hu
hushuo2018@163.com

Full list of author information is available at the end of the article

© The Author(s) 2025. **Open Access** This article is licensed under a Creative Commons Attribution-NonCommercial-NoDerivatives 4.0 International License, which permits any non-commercial use, sharing, distribution and reproduction in any medium or format, as long as you give appropriate credit to the original author(s) and the source, provide a link to the Creative Commons licence, and indicate if you modified the licensed material. You do not have permission under this licence to share adapted material derived from this article or parts of it. The images or other third party material in this article are included in the article's Creative Commons licence, unless indicated otherwise in a credit line to the material. If material is not included in the article's Creative Commons licence and your intended use is not permitted by statutory regulation or exceeds the permitted use, you will need to obtain permission directly from the copyright holder. To view a copy of this licence, visit http://creativecommons.org/licenses/by-nc-nd/4.0/.

Introduction

Colorectal cancer (CRC) is the third most common cancer worldwide and the second leading cause of cancer-related deaths [1]. Oxaliplatin (Oxa) is a first-line chemotherapeutic agent for advanced CRC treatment [2]. Although oxaliplatin-based adjuvant chemotherapy significantly improves patient prognosis, approximately 50% of patients rapidly develop resistance during treatment, leading to refractory disease and severely limiting its clinical application [3]. In cancer therapy, when drug-induced reactive oxygen species (ROS) levels exceed a critical threshold, cell toxicity occurs, curbing cancer progression. However, tumors develop adaptive mechanisms to counteract ROS - induced oxidative damage. In CRC, intracellular ROS levels drop while nicotinamide phosphoribosyltransferase (NAMPT) expression rises [4, 5]. NAMPT, a key enzyme in nicotinamide adenine dinucleotide (NAD^+) biosynthesis, causes elevated NAD^+ levels when overexpressed. This boosts NAD^+ - dependent metabolism and antioxidant defense systems (ADS), reducing cellular ROS and leading to oxaliplatin resistance [4–7], posing a significant challenge in CRC therapy. Given the strong NAD - related ADS and limited ROS substrates in resistant cells, ROS - induced therapy is restricted. Currently, no therapeutic strategies directly targeting NAD^+ degradation are available. Clinical approaches have primarily focused on reducing NAD^+ levels by inhibiting NAMPT activity. However, severe adverse effects observed in Phase I/II clinical trials, along with the emergence of primary or acquired resistance, have greatly hindered the clinical application of NAMPT inhibitors [8–11]. Therefore, the development of safe and effective therapeutics specifically targeting NAD^+ in tumor cells represents a critical clinical opportunity.

The convergence of nanotechnology and enzymology has revolutionized biomedical research through the emergence of nanozymes-engineered nanomaterials exhibiting intrinsic catalytic properties analogous to natural enzymes. Nanozymes structurally integrate enzyme-like active centers and electron-transfer systems while maintaining the inherent physicochemical advantages of nanomaterials [12]. These bioinspired catalysts demonstrate classical enzymatic activities including peroxidase (POD) and oxidase (OXD) functions, enabling the generation of cytotoxic ROS– such as singlet oxygen ($^1O_2$), superoxide anion radicals ($\bullet O_2^-$), and hydroxyl radicals ($\bullet OH$)– for effective tumor microenvironment modulation [13]. More significantly, they possess the unique enzymatic capability to mimic nicotinamide adenine dinucleotide (phosphate) oxidases (NOX), directly catalyzing the oxidation of metabolic coenzymes NAD(P)H to $NAD(P)^+$. This enzymatic intervention effectively disrupts cellular redox homeostasis and impairs mitochondrial ATP synthesis, thereby starving tumor cells of essential energy supplies [14, 15]. However, merely oxidizing NADPH and NADH is inadequate, as the resulting $NADP^+$ and NAD^+ contribute to DNA repair and mitochondrial activation, which restores NADPH and NADH levels [16]. This limitation underscores why current antimetabolic therapies often fail to fully disrupt tumor metabolism [17, 18]. Targeting NAD^+ for rapid degradation offers a novel strategy to inhibit tumor metabolism, as NAD^+ serves as a precursor for $NADP^+$ synthesis. Recently, various metal oxide-based nanozymes with different enzyme-mimicking activities have been developed for cancer treatment research [19]. However, the limited diversity of active sites and the high energy barriers of catalytic intermediates at metal sites significantly constrain the catalytic efficiency and clinical applicability of single-metal oxide nanozymes [20]. Building on this foundation, recently developed bimetallic oxide-based nanozymes exhibit more diverse active sites, including two distinct metal sites with synergistic catalytic effects and isolated active sites formed by different bimetallic atoms [17]. These nanozymes demonstrate improved stability and enhanced catalytic activity [21]. However, optimizing the structure and composition of nanozymes based on their catalytic functions to achieve maximum catalytic activity and stability remains a significant challenge.

The catalytic performance of bimetallic nanozymes is primarily reflected in their catalytic activity and stability. The reaction rate and selectivity can be effectively tuned by adjusting external potentials. Additionally, modifying surface defect sites enhances the adsorption capacity of reactive groups and increases the exposure of active sites, thereby improving both catalytic activity and stability [22]. Furthermore, oxygen vacancies (OVs)—intrinsic defects in metal oxides caused by the removal of oxygen ions from the lattice—play a critical role in influencing the catalytic activity and stability of bimetallic nanozymes. These vacancies provide coordinatively unsaturated sites and unpaired electrons, enhancing electron-hole separation, molecular activation, and electron transfer [23, 24]. Recent studies have demonstrated that the nitrogen atom within the pyridine ring of NAD^+ has a high affinity for free electrons. Once this nitrogen atom accepts free electrons, it can trigger either glycosidic bond cleavage or rearrangement of conjugated bonds, both of which ultimately result in the decomposition of NAD^+ [25]. Therefore, constructing OV-engineered bimetallic nanozymes for NAD^+ degradation holds great potential and feasibility. Recently, copper ions, an essential trace element for the human body, have been identified as a crucial component of natural NADH oxidase [26]. Copper-based nanozymes can generate potent and diverse ROS while their copper sites exhibit strong intrinsic substrate adsorption capabilities,

effectively lowering the energy barriers of reaction intermediates. Additionally, copper-based nanozymes enhance catalytic activity by modulating electronic interactions with adjacent atoms [27, 28], making them highly suitable for constructing bimetallic nanozymes designed for NAD^+ degradation. Introducing manganese ions into copper-based nanozymes not only enables multi-enzyme mimetic activities within the tumor microenvironment (TME) but also mitigates potential long-term toxicity by decomposing in response to the TME [29]. Thus, leveraging the properties of these semiconductor oxides and introducing oxygen vacancies with unique electron configurations to promote electron transfer and enhance NAD^+ catalytic degradation is a promising strategy. The mechanisms underlying this enhancement warrant further investigation.

Based on these principles, we developed $CuMnO_{x-V}$@Oxa@SP, a bimetallic oxide nanozyme enriched with OVs, modified with soybean phospholipid (SP), and loaded with oxaliplatin (Scheme 1A). This multifunctional system exhibits POD- and OXD-like activities, as well as unique nanoNAD-mimetic properties, irreversibly decomposing NAD^+ into ADP-ribose radicals and nicotinamide (NAM), thereby blocking NAD^+ synthesis and disrupting the electron transport chain. These disruptions halt the tricarboxylic acid (TCA) cycle, reduce NADH and ATP production, and restore chemosensitivity to oxaliplatin, enhancing DNA damage and apoptosis (Scheme 1B). Furthermore, OVs weaken the O-O bond in H_2O_2, enhancing ROS generation. $CuMnO_{x-V}$@Oxa@SP converts H_2O_2 into hydroxyl radicals (•OH) via POD-like activity and O_2 into superoxide anion ($•O_2^-$) via OXD-like activity, generating singlet oxygen ($^1O_2$) under acidic conditions. Transcriptomic analysis revealed downregulation of the oxaliplatin resistance-related gene glutathione S-transferase P1 (GSTP1), increasing oxaliplatin accumulation and efficacy. This is the first reported use of OV-enriched, biodegradable nanozymes with NAD^+ oxidase-like activity for cancer therapy, offering a promising strategy for oxaliplatin-resistant CRC.

Materials and methods

Preparation of $CuMnO_{x-V}$

$(Cu(acac)_2)$ (0.261 g, 1.0 mmol), $(Mn(acac)_3$ (0.253 g, 1.0 mmol), and TEG (100 mL) were mixed with the aid of bath sonication, then slowly heated to reflux over 3 h under a nitrogen atmosphere. After cooling down, EA (20 mL) was added to the blackish homogeneous suspension, which was mixed by magnetic stirring. The nanoparticles were collected by centrifugation (8000 rpm, 10 min) and washed with EA 5 times, then dried in vacuo to give a blackish solid (0.15 g).

Preparation of $CuMnO_{x-V}$@Oxa

1.0 mg/ml Oxaliplatin (Oxa) DMF solution (5 ml) was added into the solution of $CuMnO_{x-V}$ and stirred for 36 h in the dark at room temperature. Finally, the nanoparticles were purified by centrifugation (10000 rpm, 10 min) to remove the unloaded free Oxa. The Oxa loading contents were calculated by ICP-MS.

Preparation of $CuMnO_{x-V}$@Oxa@SP

To improve the biocompatibility of $CuMnO_{x-V}$@Oxa, soybean phospholipid (SP) was used to modify the surface of $CuMnO_{x-V}$@Oxa ($CuMnO_{x-V}$@Oxa@SP). Briefly, 10 mg of $CuMnO_{x-V}$@Oxa dispersed in ethanol (10 mL) were added into 10 mL of SP in DCM solution (10 mg mL^{-1}). The mixture was stirred at 25 ℃ for overnight, and then, the product was collected by centrifugation (11000 rpm, 10 min). Finally, the $CuMnO_{x-V}$@Oxa@SP was washed with DCM five times and phosphate buffer saline (PBS) three times to remove the free SP, the $CuMnO_{x-V}$@Oxa@SP was collected with improved solubility, stability, and biocompatibility.

Cell lines

Human CRC cell line HCT116 and its corresponding oxaliplatin-resistant variant, HCT116L/OHP (HCT116/L), were obtained from the Cancer Research Institute at Central South University. Cells were cultured in Dulbecco's Modified Eagle's Medium (DMEM, Gibco, USA) supplemented with 10% fetal bovine serum (FBS, ExCell Bio, China) at 37 °C in a 5% CO_2 atmosphere. The medium was also supplemented with Penicillin-Streptomycin Solution (biosharp, China) to a final concentration of 100 U/mL and 100 μg/mL, respectively. The culture medium for HCT116/L additionally included 10 μg/mL oxaliplatin (MCE, USA) to maintain its resistance characteristics.

Intracellular degradation of NAD^+/NADH by $CuMnO_{x-V}$@Oxa@SP

HCT116/L cells were seeded at a density of 1×10^6 cells per well in 6-well plates and cultured for 24 h. Treatments were administered using different formulations: (1) PBS, (2) Oxaliplatin 20 μg/mL, (3) Oxaliplatin 40 μg/mL, (4) $CuMnO_{x-V}$@SP 100 μg/mL, and (5) $CuMnO_{x-V}$@Oxa@SP 100 μg/20μg/mL. After 24 h, the cells were washed three times with PBS, counted, and their NAD^+/NADH levels were measured using the NAD^+/NADH Assay Kit (Beyotime Biotechnology, China).

Cellular ATP content assay

Cells were seeded at a density of 1×10^6 cells per well in 6-well plates and cultured for 24 h. Following this, cells were treated with various formulations for an additional 6 hours. ATP levels were then quantified using

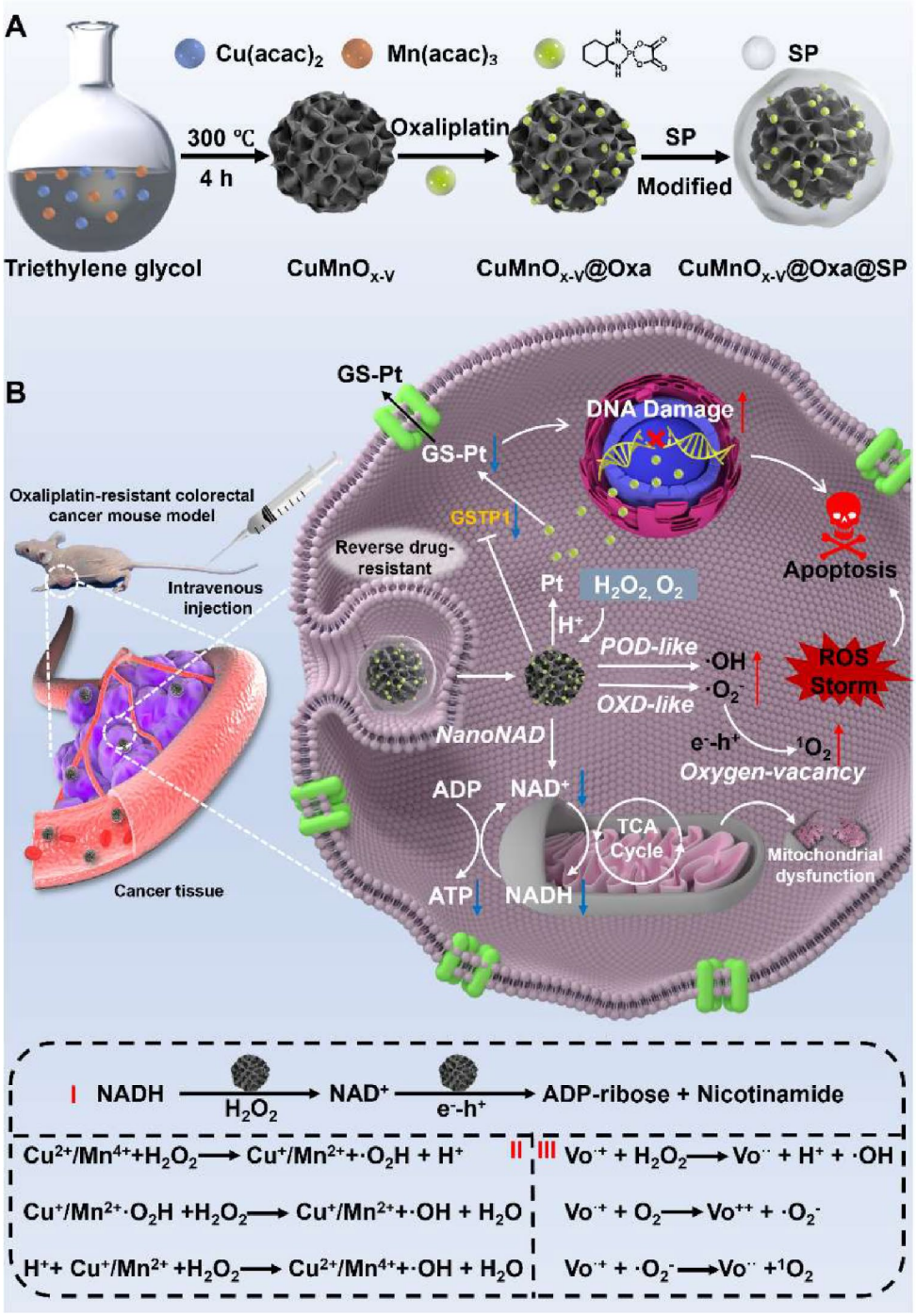

Scheme 1 Schematic illustration of (**A**) the preparation of $CuMnO_{x-V}$@Oxa@SP NFs and (**B**) $CuMnO_{x-V}$@Oxa@SP NFs exhibit multiple enzyme-mimicking activities, delivering the chemotherapeutic drug oxaliplatin while catalyzing the production of various ROS, including ·OH, $·O_2^-$, and $^1O_2$, to induce a ROS storm that synergistically promotes apoptosis. Additionally, they act as nanoNAD oxidases, rapidly and irreversibly depleting NAD^+ and NADH, reducing ATP production, and disrupting the electron transport chain, leading to mitochondrial dysfunction. Furthermore, the NFs downregulate GSTP1, a key detoxification enzyme in chemoresistant tumors, enhancing oxaliplatin accumulation by inhibiting its metabolism. This multiple mechanism synergistically overcomes drug resistance and enhances antitumor efficacy

the Enhanced ATP Assay Kit (Beyotime Biotechnology, China) with measurements taken on a Multimode Plate Reader (Perkin Elmer, US). Total protein was determined using the BCA Protein Assay Kit (Beyotime Biotechnology, China).

Intracellular ROS detection

HCT116/L cells were seeded in 6-well plates at a density of 1×10^6 cells per well and cultured for 24 h. After treatment with various formulations for 6 h, cells were stained using a high-sensitivity DCFH-DA ROS detection kit (Dojindo, Japan), dihydroethidium superoxide anion fluorescent probe (Beyotime, China), Singlet Oxygen Sensor Green (SOSG) (Beyotime, China), and the HKOH-1 hydroxyl radical high-sensitivity green fluorescent probe (MCE, USA). Fluorescence intensity was observed under a fluorescence microscope.

Mitochondrial membrane potential assay

HCT116/L cells were seeded at a density of 8×10^4 cells per well in a 24-well plate and cultured for 24 h. Cells were then exposed to various treatments for 6 h. Following exposure, cells were washed repeatedly with PBS. The mitochondrial membrane potential was evaluated using the JC-1 Kit (Beyotime Biotechnology, China). Fluorescence intensity was observed under a fluorescence microscope.

Immunofluorescence staining

HCT116/L cells were seeded at a density of 8×10^4 cells per well in a 24-well plate pre-equipped with coverslips and cultured for 24 h. After this period, cells were treated with various formulations for an additional 6 h. Following treatment, cells were rinsed, fixed, and permeabilized. Overnight incubation at 4°C was done with a primary antibody against γH2AX (#9718, Cell Signaling Technology, USA) at a dilution of 1:400. Secondary antibody incubation was performed at room temperature for 1 h. After washing off the secondary antibody, coverslips were mounted using a DAPI-containing mounting medium (Abcam, UK). Fluorescence microscopy was employed to examine the samples.

Western blot

Protein samples extracted from treated HCT116/L or HCT116 cells were separated using 8% sodium dodecyl sulfate-polyacrylamide gel electrophoresis (SDS-PAGE). After transferring onto a PVDF membrane, the samples were blocked and incubated overnight at 4 °C with primary antibodies against NAMPT (1:1000, ab236874, abcam, UK), GSTP1(1:1000, ab138491, abcam, UK), and GAPDH (1:5000, ab8254, abcam, UK). HRP-conjugated secondary antibodies were then applied. Protein blots were visualized using the ChemiDoc XRS + System (BIO-RAD, USA) and analyzed with ImageJ.

Animal model

Healthy female BALB/c nude mice, aged 5 weeks, were procured from the Department of Laboratory Animals of Central South University. All animal procedures were approved by the Institutional Animal Care and Use Committee (IACUC) (Certificate No. 20220533), The Second Xiangya Hospital, Central South University. Subcutaneous injection of 5×10^6 HCT116/L cells into the left flank established an HCT116/L CRC xenograft model in these mice.

Histopathology and TUNEL staining

Paraffin-embedded tumor tissue sections were subjected to immune-histochemical staining. Sections were heated at 60 °C, followed by blocking with 10% goat serum. They were then incubated overnight with Ki67 primary antibody (1:2000, 27309-1-AP, Proteintech, US), followed by a secondary antibody incubation and subsequent color development. Nuclei were stained with hematoxylin, and slides were examined under a microscope. Cell apoptosis was quantified using a colorimetric terminal deoxynucleotidyl transferase-mediated dUTP nick end labeling (TUNEL) apoptosis assay kit (Beyotime, China), following the manufacturer's instructions.

Statistical analysis

All statistical analyses were performed using GraphPad Prism 9 (GraphPad Software, USA). Quantitative data are presented as mean ± standard deviation (SD). Significance between groups was determined using two-tailed Student's t-tests and one-way ANOVA. Significance thresholds were set at: $^{*}P < 0.05$, $^{**}P < 0.01$, $^{***}P < 0.001$, $^{****}P < 0.0001$, P-value > 0.05 was considered not significant (ns).

Results

Design, synthesis, and characterization of $CuMnO_{x-V}$@Oxa@SP NFs

$CuMnO_{x-V}$ nanozyme was synthesized by a one-pot thermal decomposition method of Cu $(acac)_2$ and Mn $(acac)_3$ in trimethylene glycol (TG) at high temperature under N_2 atmosphere, and the synthetic process and structure of $CuMnO_{x-V}$ nanoflowers are shown in Fig. 1A. To enhance the physiological stability and no significant toxicity both in vitro and in vivo [30], $CuMnO_{x-V}$ NFs surface was modified with soybean phospholipid (SP). The morphologies of the $CuMnO_{x-V}$, $CuMnO_{x-V}$@Oxa, and $CuMnO_{x-V}$@Oxa@SP NFs were observed using transmission electron microscopy (TEM) (Fig. 1B and Figures S1A-S1B). TEM results showed that $CuMnO_{x-V}$ presented a flower-like nanostructure ($CuMnO_{x-V}$ NFs).

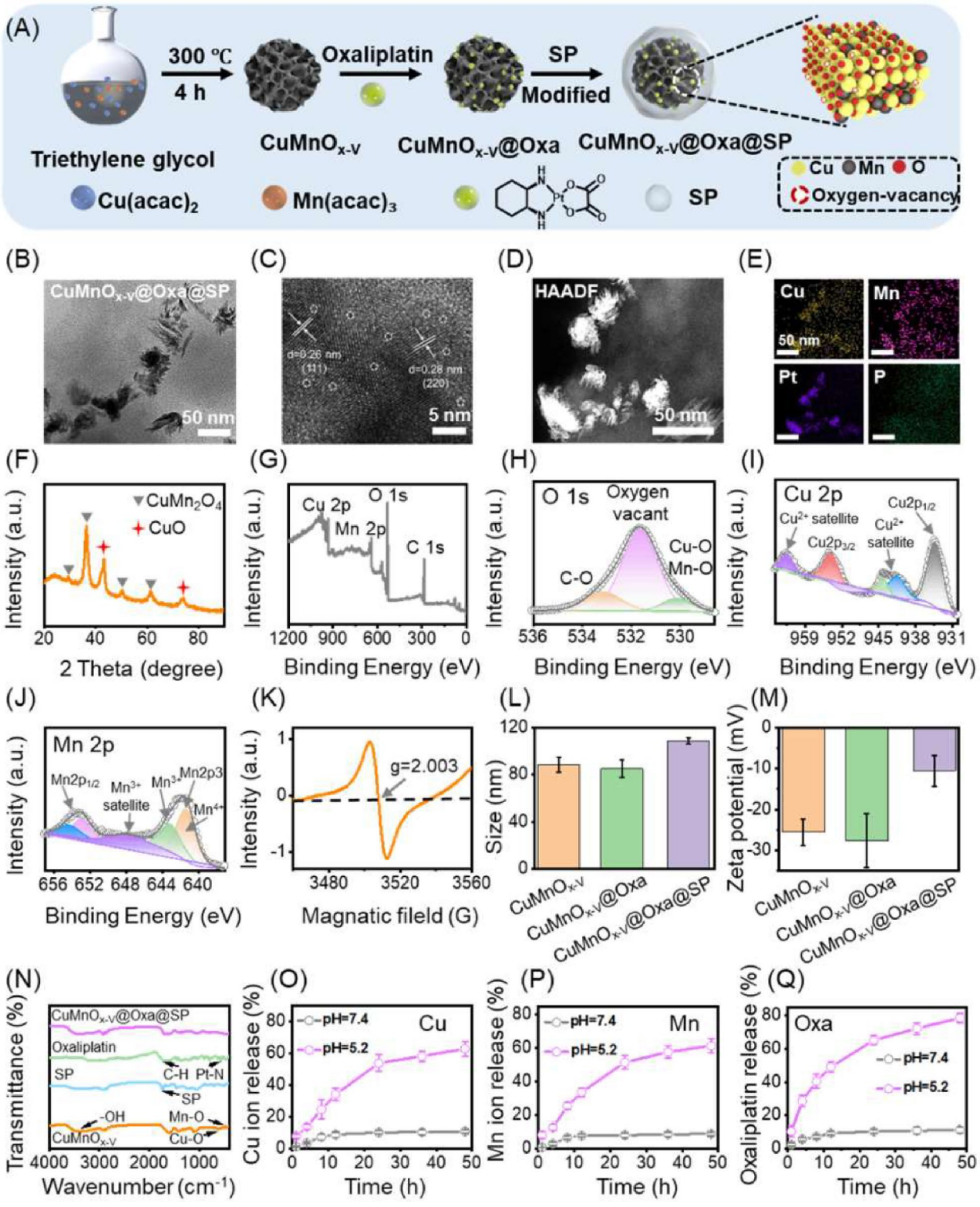

Fig. 1 Structure and properties. (**A**) Schematic diagram of the synthetic process and structure of CuMnO$_{x-V}$@Oxa@SP NFs. (**B**) TEM image, (**C**) HRTEM image, (**D**) HAADF scanning TEM images, and (**E**) The corresponding elemental mappings of CuMnO$_{x-V}$@Oxa@SP NFs. (**F**) PXRD pattern of CuMnO$_{x-V}$ NFs. (**G**) XPS survey spectra, high-resolution (**H**) O1s, (**I**) Cu 2p, and (**J**) Mn 2p spectrum of CuMnO$_{x-V}$ NFs. (**K**) ESR spectra of CuMnO$_{x-V}$ NFs. (**L**) The hydrodynamic diameter and (**M**) the Zeta potential of CuMnO$_{x-V}$ NFs, CuMnO$_{x-V}$@Oxa, and CuMnO$_{x-V}$@Oxa@SP NFs were measured in water. (**N**) FT-IR spectra of CuMnO$_{x-V}$, SP, Oxaliplatin and CuMnO$_{x-V}$@Oxa@SP NFs. pH-responsive (**O**) Cu, (**P**) Mn ions and (**Q**) Oxa release from CuMnO$_{x-V}$@Oxa@SP NFs, $n = 3$

The high-resolution transmission electron microscopy (HRTEM) image in Fig. 1C, on the one hand, apparently presents the lattice fringe spacing of 0.26 and 0.28 nm, corresponding to the (111) and (220) planes of the CuO and $CuMn_2O_4$, respectively. On the other hand, it clearly shows the defects, for instance, the dislocation faults, which are marked with white circles. The X-ray energy dispersive spectroscopy (EDS) elemental spectra demonstrated a well-proportioned distribution of Cu, Mn, Pt, and P elements, confirming the successful synthesis of $CuMnO_{x-V}$@Oxa@SP NFs (Fig. 1D and E). The crystalline structure of $CuMnO_{x-V}$ is further confirmed by X-ray diffraction (XRD) analysis. The signals corresponding to CuO and $CuMn_2O_4$ were detected on the diffraction pattern. According to JCPDS cards of CuO and $CuMn_2O_4$, peaks at 2 theta angles of 29.6 °, 36.6 °, 61.7 ° and 50.5 ° correspond to (310), (111), (220) and (311) planes of $CuMn_2O_4$ (JCPDS No. 71-1145), peaks at 2 theta angles of 43.5 ° and 74.3 °planes of CuO (JCPDS No. 44–0706), respectively (Fig. 1F).

The surface chemical state, elemental composition, and oxygen vacancies of $CuMnO_{x-V}$ were investigated via X-ray photoelectron spectroscopy (XPS). As shown in Fig. 1G and Table S1, showed a full survey scanned XPS spectra that verify the presence of the C1s (49.87%), O1s (37.28%), Mn2p (6.45%), and Cu2p (6.4%), which corresponded to peaks at 285.5, 532.1, 642.3, and 934.8 eV, respectively. For the high-resolution spectrum of Cu 2p, the peaks at 934.2, 941.4, 944.1, 953.9, and 962.3 eV correspond to Cu 2p3 Cu (I)-O, Cu 2p3 sat., Cu 2p1 Cu (II)-O and Cu 2p1 sat, respectively (Fig. 1H). The Mn 2p3 peak maximum is located in the 641.3–643.0 eV region, the peaks at 648.0 eV are assigned to Mn 2p3 sat., and the Mn 2p1 peak maximum is located in the 652.9-654.2 eV range (Fig. 1I). These peak positions were compatible with those reported for MnO_2 [31]. The three main peaks at 530.1, 531.6, and 533.14 eV in the high-resolution spectrum of O 1s are derived from lattice oxygen, oxygen vacancies, and surface oxygen, respectively (Fig. 1J). In the O 1s spectrum, the peaks at 530.1 eV and 533.1 eV correspond to the lattice oxygen in Cu-O/Mn-O bonds and surface oxygen, respectively. The high resolution XPS analysis of O 1s of $CuMnO_{x-V}$ NFs can be divided into three peaks at 530.1, 531.6 and 533.1 eV, corresponding to O^{2-} in the lattice, hydroxyl groups bonded to the metal cations in the OVs (73.4%), Cu-O/Mn-O (9.8%) and C-O (16.8), respectively (Fig. 1J and Table S2), which was consistent with the peak position of oxygen-deficient regions in previous reports [32]. More importantly, electron spin resonance (ESR) spectroscopy further verified the formation of oxygen vacancies, with an obvious signal centered at g-value 2.003 observed, which is a typical characteristic of oxygen vacancies (Fig. 1K), confirming that an OV-engineered $CuMnO_{x-V}$ NFs was successfully prepared. The presence of oxygen vacancies would promote electron-hole separation of $CuMnO_{x-V}$ in the reaction process and improve the enzyme-like catalytic performance.

The mean hydrodynamics sizes of $CuMnO_{x-V}$, $CuMnO_{x-V}$@Oxa, and $CuMnO_{x-V}$@Oxa@SP were 88.6 ± 6.5 nm, 85.3 ± 7.4 nm, and 108.9 ± 2.8 nm, respectively (Fig. 1L). With the coating of the SP, the size of $CuMnO_{x-V}$@Oxa@SP was ≈23.6 nm larger than that of $CuMnO_{x-V}$. The loading of the Oxa increased the zeta potential from − 10.5 ± 3.8 mV ($CuMnO_{x-V}$@Oxa) to -7.7 ± 2.6 mV ($CuMnO_{x-V}$@Oxa). The $CuMnO_{x-V}$@Oxa@SP had a negative zeta potential of -27.7 ± 6.6 mV due to the exposure of the free phosphate group of SP on the surface of $CuMnO_{x-V}$@Oxa (Fig. 1M). In addition, the Fourier transform infrared (FTIR) spectroscopy was used to the characteristics of the $CuMnO_{x-V}$ (Fig. 1N). The bands corresponding to the vibrations of Mn-O and Cu-O bonds appear at 492 cm^{-1} and 625 cm^{-1}, respectively. The Cu-O bands intensity in the $CuMnO_{x-V}$ shifted to higher compared to that of the Mn-O, suggesting that the formation of defects and oxygen vacancies induced Cu-O stretching vibration [19]. Moreover, the bands located at 3392 cm^{-1} belonging to OH stretching band vibrations are assigned to the stretching vibrations of -OH group of adsorbed water on $CuMnO_{x-V}$ surface. To obtain higher stability and biocompatibility, the $CuMnO_{x-V}$ surface was functionalized with SP. The peaks at 1693 cm^{-1} of $CuMnO_{x-V}$@Oxa@SP were assigned to the phosphate group vibrations of SP, suggesting the successful coating of SP onto $CuMnO_{x-V}$@Oxa. The peaks at 613 and 1713 cm^{-1} were attributed to the vibration of oxalate ligand bonds and the stretching vibration of Pt-N bond and the typical vibrations of C-H in the FTIR spectrum of $CuMnO_{x-V}$@Oxa@SP, indicating that Oxa was successfully loaded on $CuMnO_{x-V}$. Further, inductively coupled plasma mass spectrometry (ICP-MS) was performed to investigate the ion release ability of $CuMnO_{x-V}$@Oxa@SP. The release curves of Cu, Mn, and Pt ions demonstrate the acid-responsive (pH 5.2) release property (Fig. 1O, P and Q). In contrast, the released metal ions were limited at pH 7.4 after 48 h.

Multienzyme activities of $CuMnO_{x-V}$@Oxa@SP NFs

The multienzyme-mimicking activity of $CuMnO_{x-V}$@Oxa@SP NFs was evaluated for its potential in cancer therapy. The NAD^+ oxidase-like activity was evaluated by measuring the consumption of NAD^+ and NADH. (Fig. 2A) [15]. As shown in Fig. 2B, NAD^+ and NADH underwent rapid degradation within 20 min in the presence of $CuMnO_{x-V}$, with degradation rates displaying a concentration dependence. Notably, NAD^+ was consumed faster than NADH, likely due to structural similarities and interconversion between the two. Over time, both NAD^+ and NADH were almost completely depleted.

These results confirm the nano-NAD enzyme-mimicking activity of $CuMnO_{x-V}$@Oxa@SP NFs, effectively catalyzing NADH oxidation. The proposed mechanism involves NADH adsorption onto the $CuMnO_{x-V}$@Oxa@SP surface, where electron-hole pairs facilitate the two-electron oxidation of NADH into NAD•, which is further oxidized to NAD^+ or fragmented into ADP-ribose radicals and NAM (Figure S3) [33]. To further explore the impact of bimetallic nanozymes and oxygen vacancies on the NAD^+ enzyme - like activity of $CuMnO_{x-V}$@Oxa@SP NFs, we synthesized monometallic nanozymes CuO_x and MnO_x without oxygen vacancies using the same method. Under the same conditions as Fig. 2B, they couldn't catalyze NAD^+ decomposition, unlike $CuMnO_{x-V}$ (Figure S10 A-C).

To verify the reaction mechanism, NAD^+ oxidation products were analyzed by negative ion electrospray ionization mass spectrometry (ESI-MS). From the ESI-MS spectra, peaks at m/z 662.1, 558.1 and 540.1 corresponding to NAD^+, ADP-ribose and its derivatives were detected (Fig. 2C). This further evidenced the fragmentation of NAD^+ into ADP-ribose and its derivatives during NAD^+ oxidation. The observation of NAD^+ peak in Fig. 2C was almost disappeared in ESI-MS measurement. This will induce the single electron oxidation of NAD^+ into ADP-ribose and its derivatives. These results suggested that oxidation of NAD^+ involve bond cleavage, making it an irreversible process.

Next, the ROS, including •OH, $•O_2^-$ and $^1O_2$ are the three main products of multienzyme-mimicking activity, the electron spin resonance (ESR) measurement was performed to confirm their formation. We used additional colored probes that fade in response to various types of ROS to specifically distinguish the generated ROS. As shown in Fig. 2D, E, F and G, the enzyme-mimicking catalytic oxidation activity of $CuMnO_{x-V}$ NFs was evaluated using 1,3-diphenylisobenzofuran (DPBF), a yellow probe that turns colorless upon reacting with ROS. In the $CuMnO_{x-V}$ + H_2O_2 group, the characteristic DPBF absorbance peak decreased over time, reaching 20% of its initial value within 30 min, indicating efficient ROS generation. In contrast, control groups exhibited negligible DPBF degradation (Figure S4). To confirm the production of $•O_2^-$, electron spin resonance (ESR) spectroscopy with 5,5-dimethyl-1-pyrroline N-oxide (DMPO) as a radical trap revealed prominent $•O_2^-$ signals in the $CuMnO_{x-V}$ + H_2O_2 group, absent in the pure H_2O_2 group (Fig. 2G). These results indicate that the $CuMnO_{x-V}$ NFs convincingly generates $•O_2^-$ under H_2O_2. Additionally, OV-mediated $^1O_2$ generation was assessed using the singlet oxygen probe 9,10-anthracenediyl-bis(methylene) dimalonic acid (ABDA). Significant ABDA degradation occurred only in the $CuMnO_{x-V}$@Oxa@SP + H_2O_2 group (Fig. 2H-J), with characteristic $^1O_2$ signals detected via ESR (Fig. 2K), while the control groups showed no activity (Figure S5). In Fig. 2K, the pure 2,2,6,6-tetramethylpiperidine (TEMP) in the absence of $CuMnO_{x-V}$@Oxa@SP NFs were both ESR silent, the TEMP with $CuMnO_{x-V}$@Oxa@SP NFs showed three lines (1:1:1) of ESR spectra, which should be the characteristic spectra between TEMP and $^1O_2$. These results confirm that oxygen vacancies in $CuMnO_{x-V}$@Oxa@SP serve as electron donors and acceptors, facilitating $^1O_2$ generation through interactions with $•O_2^-$ (Reactions 1–2) [21].

$$oxygen\ vacancies\ (OV^{+}) + O_2 \rightarrow OV^{++} + •O_2^{-}(1).$$
$$oxygen\ vacancies\ (OV^{+}) + •O_2^{-} \rightarrow OV^{\cdot} + {}^1O_2(2).$$

Because of the variable valence Cu and Mn ions, we tested whether the $CuMnO_{x-V}$@Oxa@SP NFs, as POD-like nanozymes, could convert H_2O_2 into highly toxic •OH via the classic Fenton reaction. Accordingly, methylene blue (MB) was used as a probe to detect •OH generation. As shown in Fig. 2L, under mildly acidic conditions (pH = 5.2), MB is oxidized by the highly reactive •OH, resulting in colorless MB-OH. The •OH generation was evaluated via ESR spectroscopy using 5,5-dimethyl-1-pyrroline-N-oxide (DMPO) as an •OH trapping agent. A quadruple resonance peak with a signal intensity ratio of 1:2:2:1, a characteristic DMPO-•OH adduct, was clearly observed, indicating that $CuMnO_{x-V}$@Oxa@SP was able to convert H_2O_2 into highly toxic •OH (Fig. 2O). The characteristic peak of MB in the MB + H_2O_2 + $CuMnO_{x-V}$@Oxa@SP group faded significantly over 5 min, highlighting the excellent •OH -generating capability, verifying the POD-like activity of $CuMnO_{x-V}$@Oxa@SP (Fig. 2M and N). In contrast, the characteristic MB peak at 660 nm remained almost unchanged in the other control group (Figure S6). The acid-mediated generation of •OH by $CuMnO_{x-V}$@Oxa@SP NFs could be ascribed to the oxidation of the oxidation state Cu^{2+}/Mn^{4+} to Cu^{+}/Mn^{2+} by H_2O_2 in the presence of H^+. According to Figure S2, the ESR signal intensities were enhanced when concentration of $CuMnO_{x-V}$ increased. Taken together, these results confirm that the $CuMnO_{x-V}$ NFs produces •OH, $•O_2^-$ and $^1O_2$ under H_2O_2. These findings highlight the significance of oxygen-vacancy-engineered engineering in enhancing the catalytic performance of bimetallic nanozymes.

Density functional theory calculations on catalytic mechanism

Compared to $CuMnO_x$, the introduction of oxygen vacancy defects significantly enhances the enzyme-like catalytic activities of $CuMnO_{x-V}$, and the underlying mechanism deserves in-depth investigation. To understand the influential mechanism of oxygen vacancy defects on nanoNAD-like, OXD-like and POD-like

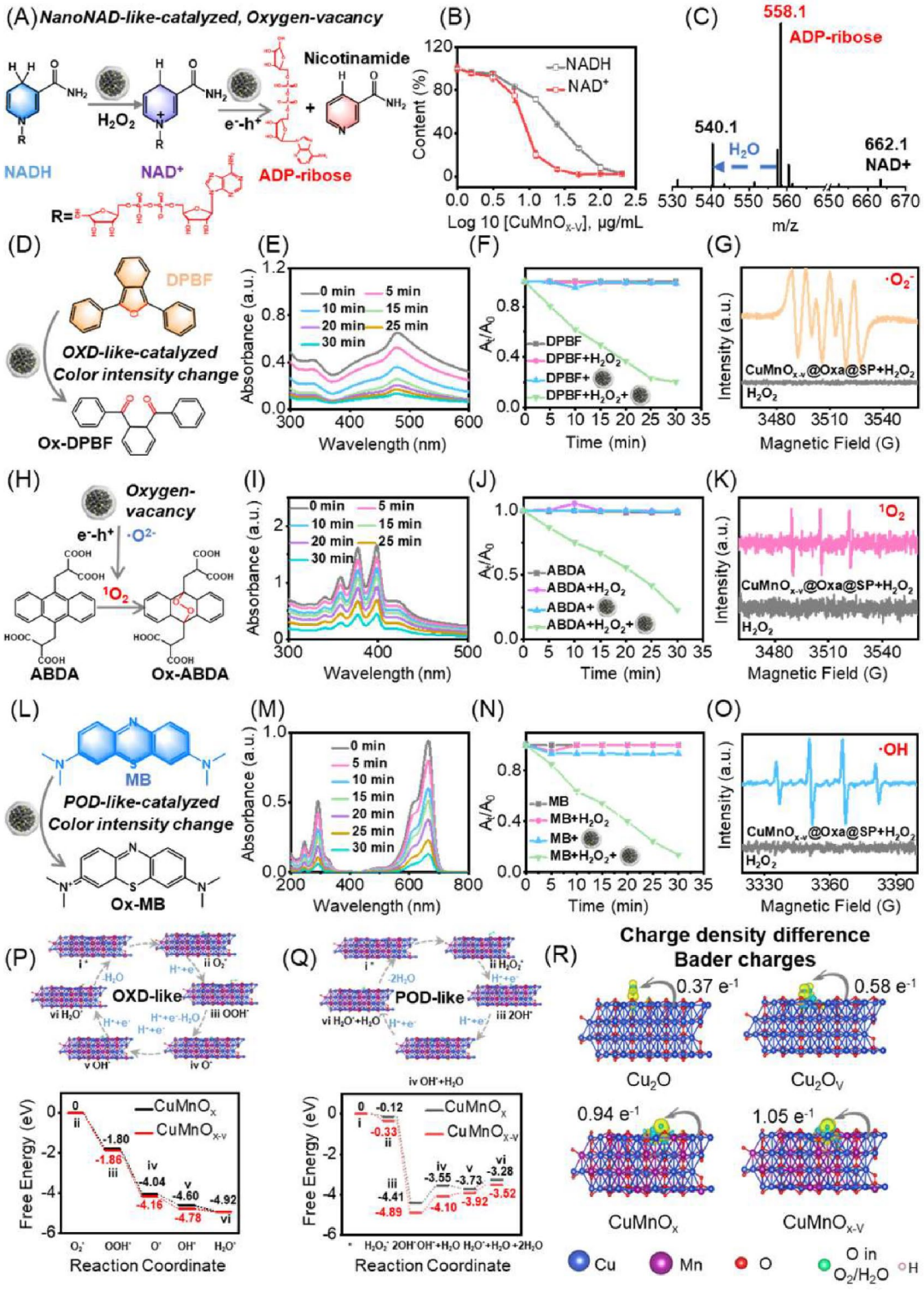

Fig. 2 (See legend on next page.)

activities more clearly, the density functional theory (DFT) calculations were executed to evaluate the potential catalytic mechanisms of $CuMnO_x$ and $CuMnO_{x-V}$. The reaction pathways and energy profiles for the POD-like activity of $CuMnO_{x-V}$ are illustrated in Fig. 2P. For the OXD-like reaction, the first step is the O_2 adsorption and then hydrogenation to generate OOH* species with an adsorption energy of -1.80 eV. A O* species

(See figure on previous page.)

Fig. 2 Multienzyme-mimicking activities of $CuMnO_{x-V}$@Oxa@SP NFs. (**A**) Schematic illustration of nanoNAD-like-catalyzed activity. (**B**) Efficiency of $CuMnO_{x-V}$@SP nanozymes in catalyzing the degradation of NADH and NAD^+ solution at various concentrations ($n = 3$). (**C**) The negative ion ESI-MS of enzymatic oxidation product of NAD^+. (**D**) Schematic illustration of the OXD-mimicking catalytic procedure of $CuMnO_{x-V}$@Oxa@SP NFs. (**E**) Detection of ROS production of $CuMnO_{x-V}$@Oxa@SP NFs + H_2O_2 groups via degradation of DPBF. (**F**) Comparison of the oxidation of DPBF among the DPBF, DPBF + H_2O_2, DPBF + $CuMnO_{x-V}$@Oxa@SP and DPBF + H_2O_2 + $CuMnO_{x-V}$@Oxa@SP. (**G**) ESR of $CuMnO_{x-V}$@Oxa@SP NFs trapped by DMPO. (**H**) Schematic illustration of ABDA catalytic activity. (**I**) Detection of $^1O_2$ production of $CuMnO_{x-V}$@Oxa@SP NFs + H_2O_2 groups via degradation of ABDA. (**J**) Comparison of $^1O_2$ production among the ABDA, ABDA + H_2O_2, ABDA + $CuMnO_{x-V}$@Oxa@SP and ABDA + H_2O_2 + $CuMnO_{x-V}$@Oxa@SP. (**K**) ESR of $CuMnO_{x-V}$@Oxa@SP NFs trapped by TEMP. (**L**) Schematic illustration of the POD-mimicking catalytic procedure of $CuMnO_{x-V}$@Oxa@SP NFs. (**M**) Detection of ROS production of $CuMnO_{x-V}$@Oxa@SP NFs + H_2O_2 groups via degradation of MB. (**N**) Comparison of the oxidation of MB among the MB, MB + H_2O_2, MB + $CuMnO_{x-V}$@Oxa@SP, and MB + H_2O_2 + $CuMnO_{x-V}$@Oxa@SP. (**O**) ESR of $CuMnO_{x-V}$@Oxa@SP NFs trapped by DMPO. DFT calculations reaction pathways and corresponding free energy diagrams of (**P**) OXD-like reaction and (**Q**) POD-like reaction for $CuMnO_x$ and $CuMnO_{x-V}$ nanozymes. (**R**) Charge density difference and Bader charges of

intermediate was created when H^+ ions approached and bonded to the adsorbed OOH* intermediate on the Cu atom (-4.16 eV). This stage resulted in energy losses of 2.3 eV. Then O* adsorbed on the Cu-Mn atom, and exutive hydrogenation steps to obtain an H_2O molecule. These two stages resulted in energy losses of 0.62 and 0.14 eV, respectively. This step in OXD-like reaction is formation process of adsorbed H_2O* molecule, which is easier for $CuMnO_{x-V}$ relative to $CuMnO_x$ counterpart.

Regarding the POD-like activity, the proposed reaction pathways and calculated energy profiles are shown in Fig. 2Q. The H_2O_2 molecule is first adsorbed on the surfaces of $CuMnO_x$ and $CuMnO_{x-V}$ with surface adsorption energies of -0.12 and − 0.33 eV, respectively, which makes it easy for H_2O_2 to adsorb on the surface of both samples. H_2O_2 molecule was captured by the $CuMnO_{x-V}$ and adsorbed on a Cu atom, indicating that the binding of H_2O_2 to the $CuMnO_{x-V}$ was energetically favorable. Subsequently, the absorbed H_2O_2 molecule is uniformly cleaved by Cu-Mn* to form surface-active groups attached to Cu-Mn. Most noteworthy, the defective formation of oxygen vacancies in $CuMnO_{x-V}$ results in a strong adsorption capacity, which makes it difficult for H_2O_2 molecules to stabilize on the $CuMnO_{x-V}$ surface, thus dissociating directly into 2OH* (-4.89 eV) with low energy. Subsequently, an increase in energy (-4.10 eV) occurred as a result of the release of OH*, and the other OH* species reacted with the approaching H^+ to form H_2O adsorbed on the surface, with an energy drop of -3.92 eV. Finally, $CuMnO_{x-V}$ recovered with an energy increase of -3.52 eV following the formation of the products. These results also explain that oxygen defects reduce the free energy in OXD-like and POD-like reactions, and their moderate binding on the nanozyme surface is beneficial for accelerating the catalytic reactions observed in this study.

To further illustrate atomic interface structure on the electron properties of $CuMnO_{x-V}$, we investigated charge density difference and Bader charge analysis. The Cu_2O, Cu_2O_V, $CuMnO_x$ and $CuMnO_{x-V}$ were chosen asananalysis model to discuss their performance in enzyme-like catalysis (Fig. 2R). The adsorbed H_2O_2 species on $CuMnO_{x-V}$ gained a notably higher quantity of electrons (1.05 e^{-1}) than on $CuMnO_x$ (0.94 e^{-1}), Cu_2O_V (0.58 e^{-1}) and Cu_2O (0.37 e^{-1}). From this result, the energy barriers of Cu-Mn dual-metal oxide is absolutely lower than that of Cu single-metal oxide, which suggests that the dual-metal oxide is more favorable for generating •OH compared to the two single-metal oxide, and that of oxygen defect rich Cu-Mn dual-metal oxide is the lowest. Furthermore, the introduction of oxygen vacancy defects alters the electron properties of $CuMnO_{x-V}$, regulates the binding of OH* intermediate on nanozyme surface and finally obtains optimized enzyme-like catalytic reaction processes. These results further validates that the combined effect of Cu-Mn dual-metal sites and oxygen vacancy defects facilitates the separation and transfer of electrons and holes during the enzyme-like catalytic reaction process on $CuMnO_{x-V}$, which is consistent with above findings.

Intracellular NAD^+ pool expansion as a key mechanism of oxaliplatin resistance in colorectal cancer

To investigate the mechanisms of oxaliplatin resistance in colorectal cancer, we utilized the oxaliplatin-resistant cell line HCT116/L. The half maximal inhibitory concentration (IC50) of oxaliplatin in HCT116/L cells was 27.08 μg/mL, compared to 5.99 μg/mL in parental HCT116 cells (Fig. 3A). NAD^+ levels in HCT116/L cells were ~ 5.4 times higher than in HCT116 cells, primarily due to elevated NAMPT expression driving the salvage pathway (Fig. 3B-E). Elevated NAD^+ enhances cancer cell survival by supporting DNA repair, antioxidant responses, and metabolic reprogramming. To clarify the role of NAD^+, we modulated its levels in HCT116 cells. NAM/D-Rib (D-Ribose) supplementation increased NAD^+ and oxaliplatin resistance in a concentration-dependent manner, while the NAMPT inhibitor FK866 reversed resistance and restored sensitivity to oxaliplatin (Fig. 3F-J, Figure S7). Flow cytometry confirmed that elevated NAD^+ suppressed apoptosis, whereas FK866 synergistically enhanced oxaliplatin-induced apoptosis (Fig. 3K-L). In HCT116/L cells, FK866 exhibited strong synergy with oxaliplatin (ZIP synergy score: 7.1),

effectively overcoming resistance. However, these cells were less sensitive to FK866 due to their higher NAD^+ levels, which prolonged metabolic activity and survival despite salvage pathway inhibition (Figure S8A-D).

Cellular uptake of $CuMnO_{x-V}$@SP

Effective cellular uptake is critical for the tumor accumulation of nanozymes, as sufficient accumulation within tumor cells is necessary to ensure their therapeutic effects through localized catalytic activity. Indocyanine green (ICG)-labeled $CuMnO_{x-V}$@SP nanozymes $CuMnO_{x-V}$@ICG@SP showed time-dependent uptake in oxaliplatin-resistant HCT116/L cells, confirmed by increasing red fluorescence via confocal laser scanning microscope (Figure S9A-B). Predominantly localized in lysosomes (Figure S9C), the acidic lysosomal environment enhanced peroxidase-like activity, boosting antitumor effects during oxaliplatin treatment [34, 35].

In vitro NAD-like catalytic activities of $CuMnO_{x-V}$@Oxa@SP

The interconversion of NAD^+ and NADH in tumor cells is driven by glycolysis and the mitochondrial TCA cycle. However, traditional NOX-based therapies, which accelerate NADH-to-NAD^+ conversion, primarily reduce ATP production without fully disrupting the mitochondrial ETC or blocking NAD^+ resynthesis via the salvage pathway, limiting their efficacy. Degrading NAD^+ into NAM and ADP-ribose, which cannot re-enter the salvage pathway, is critical for halting ETC activity and promoting apoptosis (Fig. 4A). In HCT116/L cells treated with 100 μg/mL $CuMnO_{x-V}$@SP, NAD^+ was rapidly degraded, while NADH showed a slower, time-dependent decline (Fig. 4B). By 48 h, when most cells had died, NAD^+ and NADH levels equaled those in the culture medium. A 24-hour incubation period was chosen for subsequent experiments. As shown in Fig. 4C-D, treatment with $CuMnO_{x-V}$@SP significantly reduced NAD^+ and NADH levels compared to the PBS group. In contrast, 40 μg/mL oxaliplatin increased NAD^+ and NADH levels, likely due to stress responses stimulating their production as a protective mechanism. These results highlight the capability of $CuMnO_{x-V}$@SP to effectively disrupt NAD^+ metabolism, offering a novel strategy to combat drug-resistant tumors. Notably, monometallic nanozymes CuO_x and MnO_x also have NOX - like activity. Compared with the control group, they can reduce intracellular NADH content (Figure S10D). However, they can't degrade intracellular NAD^+. Instead, due to NADH oxidation, there's a tendency for NAD^+ content to increase (Figure S10E).

To further investigate the efficiency of NAD^+ oxidation and degradation by $CuMnO_{x-V}$@SP and $CuMnO_{x-V}$@Oxa@SP, as well as the duration of salvage pathway inhibition, we employed a single low-dose treatment approach. This ensured that tumor cells would not undergo complete cell death, allowing the experiment to proceed without premature termination. The medium was partially refreshed every two days to maintain experimental conditions. We then monitored the changes in NAD^+ levels over time in HCT116/L cells following treatment with $CuMnO_{x-V}$@SP or $CuMnO_{x-V}$@Oxa@SP. Interestingly, before 48 h, NAD^+ levels in the $CuMnO_{x-V}$@Oxa@SP group were slightly higher than those in the $CuMnO_{x-V}$@SP group. After 48 h, $CuMnO_{x-V}$@Oxa@SP effectively continued to deplete NAD^+ and inhibit its synthesis, while NAD^+ levels in the $CuMnO_{x-V}$@SP group gradually increased (Fig. 4D). This can be attributed to partial biodegradation of $CuMnO_{x-V}$@SP at low doses, reducing its NAD^+-consumption efficiency. Additionally, NAD^+ precursors introduced through medium replenishment reactivated the salvage pathway. Nonetheless, NAD^+ levels remained relatively low even after 144 h. The $CuMnO_{x-V}$@Oxa@SP group demonstrated remarkable efficiency in depleting NAD^+ and inhibiting its synthesis, likely due to the synergistic effect between oxaliplatin and the nanoNADase activity. NAD^+ depletion exacerbated oxaliplatin-induced DNA damage and mitigated nanozyme dilution caused by cell division, as the DNA repair process typically relies on NAD^+. Given the direct influence of NAD^+ on cellular glucose metabolism [36] and the regulation of ATP production, we further explored the effects of $CuMnO_{x-V}$@Oxa@SP on cellular glucose metabolism using ^{18}F-FDG uptake experiments. As illustrated in Fig. 4E, glucose metabolism significantly decreased in both $CuMnO_{x-V}$@SP and $CuMnO_{x-V}$@Oxa@SP groups compared to the PBS control, also exhibiting suppressed ATP production (Fig. 4F). These findings indicate that $CuMnO_{x-V}$@Oxa@SP effectively depletes NAD^+ continuously, disrupts the mitochondrial ETC, impairs tumor cell glycolysis, and inhibits ATP production.

Intracellular ROS detection

$CuMnO_{x-V}$ multifunctional nanozymes exhibit ROS-catalytic activities, including POD-like, OXD-like, and OVs-mediated activities (Fig. 4H). To evaluate their impact on oxidative stress in chemotherapy-resistant HCT116/L cells, we used DCFH-DA to measure total ROS generation after 4 h of treatment with different formulations. As shown in Fig. 4I, minimal fluorescence was observed in the PBS, 20 μg/mL oxaliplatin, and 40 μg/mL oxaliplatin groups, indicating low ROS production. In contrast, the $CuMnO_{x-V}$@SP and $CuMnO_{x-V}$@Oxa@SP groups displayed intense green fluorescence, signaling significant ROS generation due to nanozyme activity. This result suggests that $CuMnO_{x-V}$@SP enhances ROS production compared to oxaliplatin alone, likely due to the high NAD^+ levels in HCT116/L cells, which can counteract oxidative stress induced by oxaliplatin [37].

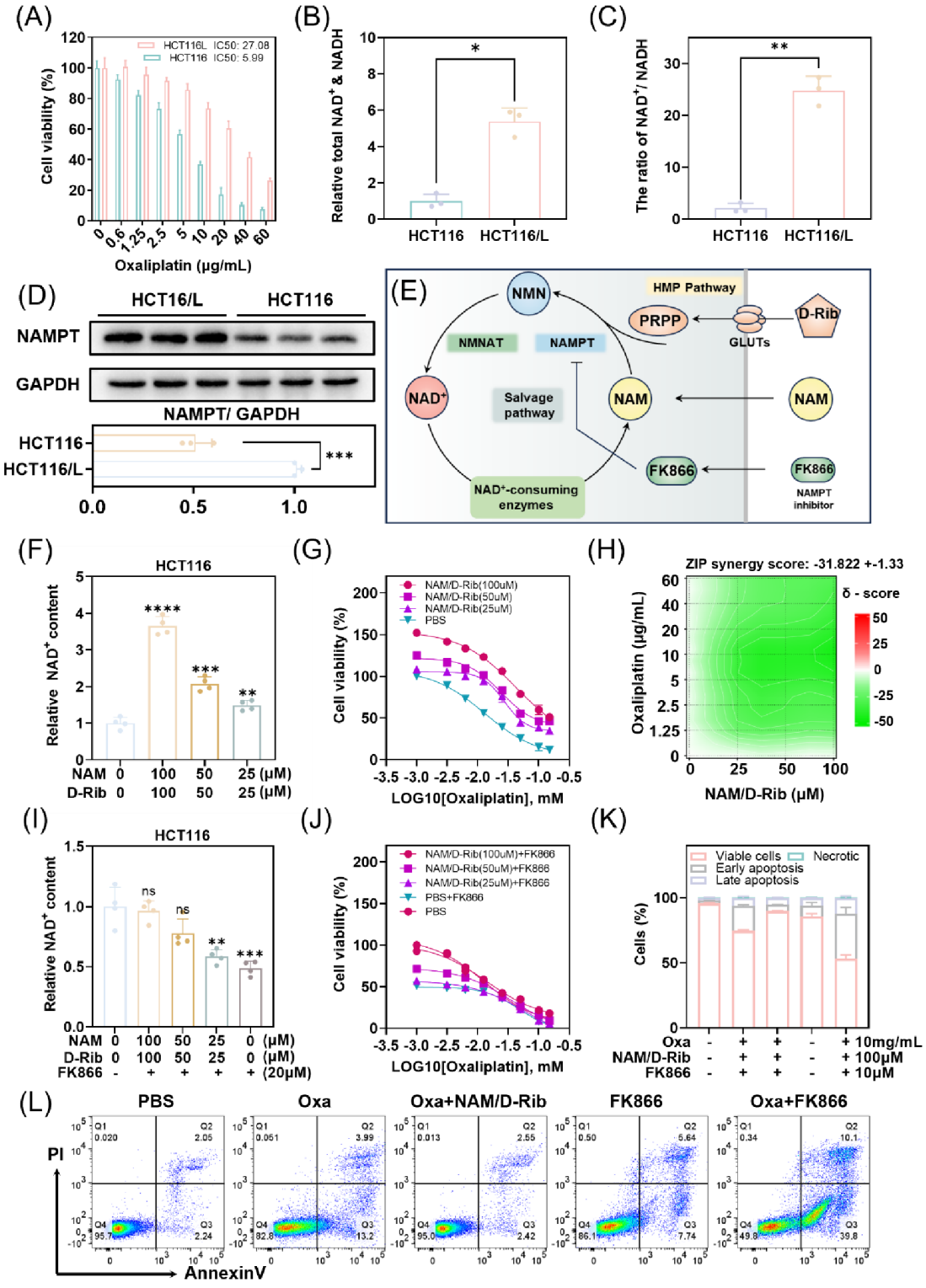

Fig. 3 (See legend on next page.)

We further confirmed the ROS-catalytic activities of $CuMnO_{x-V}$@SP by assessing the production of $\bullet O_2^-$, $^1O_2$, and •OH in treated cells. Fluorescence microscopy using specific ROS sensors revealed strong fluorescence signals only in the $CuMnO_{x-V}$@SP and $CuMnO_{x-V}$@Oxa@SP groups (Fig. 4I), indicating the nanozyme's ability to generate all three reactive species. Flow cytometry analysis quantified ROS-positive cells, revealing 68.1%

(See figure on previous page.)

Fig. 3 Intracellular NAD^+ elevation as a key mechanism of oxaliplatin resistance in colorectal cancer. (**A**) Evaluation of oxaliplatin resistance in the HCT116/L oxaliplatin-resistant colorectal cancer cell line and its parental HCT116 cell line. (**B**) Total NAD^+ and NADH levels in HCT116 and HCT116/L cells. (**C**) NAD^+/NADH ratio. (**D**) Immunoblotting and quantification of NAMPT, the rate-limiting enzyme in the NAD^+ salvage pathway, in HCT116/L and HCT116 cells. (**E**) Schematic of the NAD^+ salvage pathway in tumor cells. (**F**) Intracellular NAD^+ levels in HCT116 cells after 24-hour incubation with different concentrations of NAM/D-Rib, $n = 4$. (**G**) Cell viability of HCT116 cells co-incubated with NAM/D-Rib and oxaliplatin for 24 h. (**H**) ZIP synergy score heatmap for the effect of NAM/D-Rib on oxaliplatin sensitivity in HCT116 cells, with red indicating synergy, green indicating antagonism, and white indicating an additive effect. (**I**) Intracellular NAD^+ levels in HCT116 cells treated with FK866 + NAM/D-Rib for 24 h, $n = 4$. (**J**) Cell viability of HCT116 cells co-incubated with NAM/D-Rib, oxaliplatin, and FK866 under the same conditions as (**G**). (**K**, **L**) Flow cytometry analysis of apoptosis in HCT116 cells treated with NAM/D-Rib or FK866 for 24 h, and corresponding statistical analysis, $n = 3$. Error bars: S.D., $^*p < 0.05$, $^{**}p < 0.01$, $^{***}p < 0.001$, $^{****}p < 0.0001$

and 82.7% ROS-positive cells in the $CuMnO_{x-V}$@SP and $CuMnO_{x-V}$@Oxa@SP groups, respectively, compared to just 3.1% in the control group (Fig. 4J). These findings demonstrate that $CuMnO_{x-V}$@SP rapidly catalyzes ROS production, contributing to its potent cytotoxic effects.

Catalytic consumption of NAD^+ sensitizes oxaliplatin to enhance antitumor efficacy

Building on the robust catalytic performance of $CuMnO_{x-V}$@Oxa@SP nanozymes, we further assessed their cytotoxic efficiency against HCT116/L cells. As shown in Fig. 5A. Initially, $CuMnO_{x-V}$@Oxa@SP releases oxaliplatin, which forms cross-links with DNA, antagonizing its replication, transcription, and repair processes, thereby accumulating DNA damage. In addition, the nanozyme, utilizing its efficient enzyme-mimicking properties, catalyzes a ROS storm while rapidly degrading NAD^+, disrupting the mitochondrial ETC, and leading to mitochondrial damage, further promoting cell apoptosis. The combination of the nanozyme and oxaliplatin synergistically enhances apoptosis in HCT116/L cells.

To evaluate DNA damage, we used immunofluorescence staining for γ-H2AX, a marker for DNA double-strand breaks (Fig. 5B-C). The $CuMnO_{x-V}$@Oxa@SP group showed the strongest green fluorescence, indicating the most severe DNA damage, aligning with ROS findings. This increase in ROS and decrease in NAD^+ may cause mitochondrial damage. We assessed mitochondrial membrane potential changes with JC-1 staining. Normal high membrane potential mitochondria emit red fluorescence, while damaged ones emit green (Fig. 5D-E). The PBS, Oxa 20 μg/mL, and Oxa 40 μg/mL groups showed normal function with strong red and weak green fluorescence. However, the $CuMnO_{x-V}$@SP and $CuMnO_{x-V}$@Oxa@SP groups indicated severe damage with weak red and intense green fluorescence.

We also differentiated live and dead cells using propidium iodide (PI, red) and calcein-AM (green) to evaluate $CuMnO_{x-V}$@Oxa@SP's cytotoxicity on HCT116/L cells (Fig. 5F-G). The Oxa 20 μg/mL group had minor effects on cell viability, while the Oxa 40 μg/mL and $CuMnO_{x-V}$@SP groups showed significant cell damage with vivid red fluorescence. The $CuMnO_{x-V}$@SP group also showed increased cell death, reduced surviving cell size, and morphological changes, possibly due to the elevated NAD^+ levels in HCT116/L cells, which supports DNA repair and ADS. Oxaliplatin only mildly inhibited proliferation, but the $CuMnO_{x-V}$@SP group depleted NAD^+, causing DNA damage and oxidative imbalance. The $CuMnO_{x-V}$@Oxa@SP group showed negligible green fluorescence, suggesting reduced NAD^+ impaired DNA repair and antioxidant capabilities, increasing susceptibility to ROS and enhancing oxaliplatin's antitumor efficacy. Flow cytometry with Calcein-AM and PI dual staining (Fig. 5H-I) confirmed these results, consistent with fluorescence staining.

Subsequent analyses utilized Annexin V-FITC/PI staining to detect early apoptotic events characterized by exposure of phosphatidylserine due to loss of lipid asymmetry, while PI penetrated disrupted nuclear membranes, marking late apoptotic or necrotic cells. Annexin V-FITC/PI staining revealed significantly higher apoptotic and necrotic cell proportions in the $CuMnO_{x-V}$@Oxa@SP treatment group compared to other groups, highlighting its strong cytotoxic effects (Fig. 5J-K). To assess chemosensitivity enhancement, HCT116/L cells were treated with oxaliplatin and $CuMnO_{x-V}$@SP at varying concentrations. MTT assay results showed a dose-dependent reduction in oxaliplatin IC50 values with increasing $CuMnO_{x-V}$@SP concentrations, indicating enhanced sensitivity due to ROS production and NAD^+ depletion (Fig. 5L). SynergyFinder analysis confirmed a strong synergistic effect between $CuMnO_{x-V}$@SP and oxaliplatin, with ZIP synergy scores exceeding 10 at relevant concentration ranges (Fig. 5M).

To further evaluate the antitumor efficacy of $CuMnO_{x-V}$@Oxa@SP, oxaliplatin-resistant colorectal cancer cells (HCT116/L) were treated with varying concentrations of $CuMnO_{x-V}$@SP and oxaliplatin-loaded $CuMnO_{x-V}$@Oxa@SP. As shown in Fig. 5N, $CuMnO_{x-V}$@Oxa@SP exhibited significantly stronger inhibitory effects on HCT116/L cells compared to the $CuMnO_{x-V}$@SP group. Subsequently, we used ICP-MS analysis to compare the intracellular retention of oxaliplatin between the $CuMnO_{x-V}$@SP + 20 μg/mL oxaliplatin combination and $CuMnO_{x-V}$@Oxa@SP treatment alone. As shown in Fig. 5O, at the same oxaliplatin concentration, the intracellular Pt content in the $CuMnO_{x-V}$@Oxa@SP group was significantly higher than that in the $CuMnO_{x-V}$@SP + Oxa combination group, indicating

that $CuMnO_{x-V}$@Oxa@SP enhances oxaliplatin uptake. Interestingly, compared to free oxaliplatin treatment alone, the $CuMnO_{x-V}$@SP + Oxa combination significantly increased intracellular Pt accumulation at the same oxaliplatin concentration, suggesting that $CuMnO_{x-V}$@SP inhibits cellular metabolism of Pt.

Tumor accumulation of $CuMnO_{x-V}$@SP nanozyme and Inhibition of tumor glucose metabolism

The biodistribution of $CuMnO_{x-V}$@SP nanozymes plays a critical role in their efficacy for cancer therapy. We assessed the tumor accumulation of $CuMnO_{x-V}$@ICG@SP in HCT116/L tumor-bearing mice using in vivo fluorescence imaging. As shown in Fig. 6A, fluorescence intensity in the tumor region stabilized around 6 h post-injection, indicating rapid accumulation of $CuMnO_{x-V}$@SP in the tumor tissue. Notably, the fluorescence signal persisted in the tumor area 48 h post-injection, suggesting strong retention of $CuMnO_{x-V}$@ICG@SP within the tumor. This strong retention is beneficial for therapeutic purposes as it allows prolonged catalytic activity, enhancing the efficacy of the treatment. Quantitative analysis of the average fluorescence intensity in the tumor region confirmed this observation (Fig. 6C). At 24 h post-injection, ex vivo fluorescence imaging of tumors and major organs was performed. The imaging results (Fig. 6B) revealed significant tumor accumulation of the nanozymes, alongside normal clearance via non-target organs. Additionally, we conducted ICP-MS analysis 24 h post-injection to quantify the copper, manganese, and platinum levels across different tissues. As shown in Figure S11, the major sites of accumulation were the liver, spleen, and tumor tissue.

$CuMnO_{x-V}$@SP nanozymes were evaluated as T1-weighted magnetic resonance imaging (MRI) contrast agents due to their manganese content, demonstrating excellent superparamagnetic properties. Longitudinal relaxivity (r1) measurements revealed a concentration-dependent T1 signal enhancement, with a relaxivity value of 0.0429 μg/mL (Figure S12A-B). In vivo MRI scans in HCT116/L tumor-bearing mice showed enhanced local T1 signals in tumor tissues, peaking at 24 h post-injection and remaining significantly elevated at 48 h (Figure S12C). The contrast-to-noise ratio (CNR) increased by 4.2- and 3.3-fold at 24 and 48 h, respectively, compared to controls (Figure S12D). These findings underscore the significant tumor accumulation, optimal retention, and the therapeutic potential of $CuMnO_{x-V}$@SP as a versatile theragnostic agent in the field of oncology. $CuMnO_{x-V}$@SP rapidly accumulates within tumors and remains for an extended period, promoting sustained NAD^+ depletion and disrupting glycolysis and ATP production. To evaluate its effects on metabolism, we used pre- and post-treatment ^{18}F-FDG PET/CT scans to assess glucose metabolism in HCT116/L xenografts (Fig. 6D). Quantitative analysis (Fig. 6E-G) revealed increased glucose metabolism in the PBS group, while $CuMnO_{x-V}$@Oxa@SP treatment significantly reduced glucose metabolism. These findings demonstrate that $CuMnO_{x-V}$@Oxa@SP effectively suppresses tumor metabolism, highlighting its therapeutic potential.

Evaluation of intratumoral anti-cancer efficacy of $CuMnO_{x-V}$@SP nanozymes

To evaluate the in vivo antitumor efficacy of $CuMnO_{x-V}$@Oxa@SP, HCT116/L tumor-bearing mice were treated with PBS (G1), oxaliplatin (Oxa) 5 mg/kg (G2) or 10 mg/kg (G3), $CuMnO_{x-V}$@SP 5 mg/kg (G4), or $CuMnO_{x-V}$@Oxa@SP 5 mg/1 mg/kg (G5) via tail vein injections on days 0, 2, 4, and 6 (Fig. 7A). Tumor growth suppression was most pronounced in the $CuMnO_{x-V}$@Oxa@SP group, significantly outperforming the oxaliplatin and $CuMnO_{x-V}$@SP groups after 14 days of treatment (Fig. 7B). Tumor weights were consistent with relative tumor volume trends (Fig. 7C). Unlike Oxa-treated groups, where weight loss and anorexia reduced survival [38] (Fig. 7D-E), $CuMnO_{x-V}$@Oxa@SP-treated mice exhibited no adverse effects, highlighting its superior biocompatibility.

Histopathological analysis revealed reduced Ki-67-positive cells in $CuMnO_{x-V}$@SP and $CuMnO_{x-V}$@Oxa@SP groups, indicating suppressed proliferation (Fig. 7G-H). TUNEL staining further confirmed enhanced apoptosis in the $CuMnO_{x-V}$@Oxa@SP group compared to other treatments (Fig. 7I-J). These findings demonstrate the nanozyme's robust antitumor activity by inducing apoptosis and inhibiting proliferation.

Biocompatibility and biosafety were also assessed. Although hematoxylin and eosin (H&E) staining showed no histopathological abnormalities in major organs (Figure S13), serum biochemical analysis revealed significant liver damage in the Oxa 10 mg/kg group, as indicated by elevated alanine aminotransferase (ALT), aspartate aminotransferase (AST), total bilirubin (TBIL), and total bile acids (TBA) levels and decreased albumin (ALB) (Figure S14). Kidney and muscle damage markers, such as creatinine (CREA), uric acid (UA), and creatine kinase (CK), were also elevated (Figure S15). Myocardial enzyme analysis showed increased creatine kinase isoenzyme MB (CKMB), lactate dehydrogenase (LDH), and LDH isoenzyme 1(LDH1), particularly in the Oxa 10 mg/kg group, reflecting severe cardiac injury (Figure S16). In contrast, nanozyme-treated groups exhibited no such abnormalities, confirming the safety and reduced toxicity of $CuMnO_{x-V}$@SP and $CuMnO_{x-V}$@Oxa@SP treatments.

Visual examination of excised tumors confirmed the significant therapeutic efficacy of $CuMnO_{x-V}$@Oxa@SP (Fig. 7F). These results underscore its ability to reverse

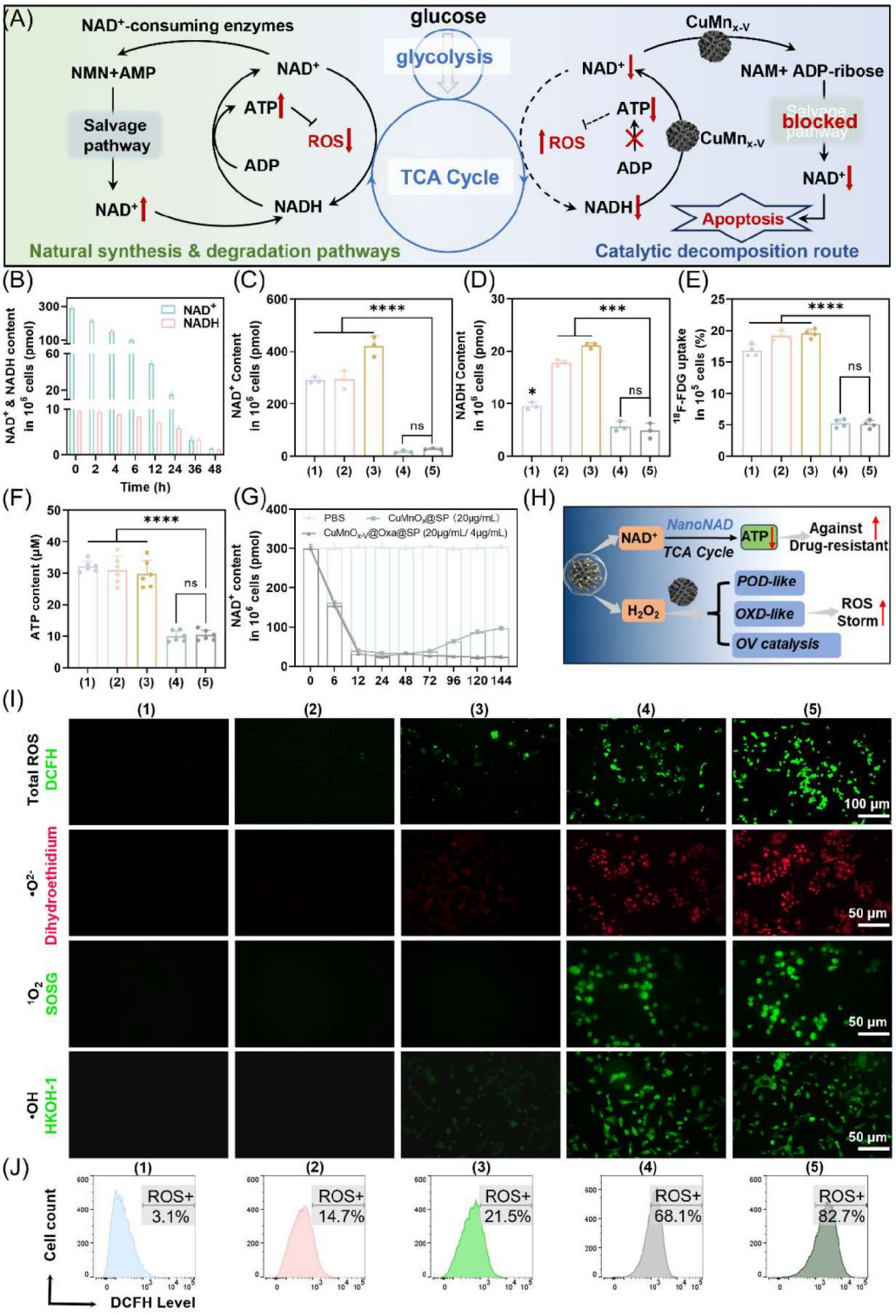

Fig. 4 In vitro evaluation of nanozyme-mimicking enzymatic performance. (**A**) Illustrates the therapeutic strategy of $CuMnO_{x-V}$@SP nanozymes irreversibly degrading NAD^+ and disrupting the electron transport chain. (**B**) NAD^+ and NADH levels in HCT116/L cells after incubation with $CuMnO_{x-V}$@SP nanozyme (100 μg/mL) for different durations. NAD^+ (**C**) and NADH (**D**) levels in HCT116/L cells treated with different methods: (1) PBS, (2) Oxa 20 μg/mL, (3) Oxa 40 μg/mL, (4) $CuMnO_{x-V}$@SP 100 μg/mL, and (5) $CuMnO_{x-V}$@Oxa@SP 100 μg/mL. (**E**) Glucose uptake and (**F**) intracellular ATP production levels in HCT116L cells under different treatments. (**G**) Duration of NAD^+ catalytic degradation in HCT116L cells following a single low-dose administration of $CuMnO_{x-V}$@SP and $CuMnO_{x-V}$@Oxa@SP. (**H**) Schematic representation of the multi-enzyme activities of $CuMnO_{x-V}$@SP nanozymes in promoting ROS generation. (**I**) Fluorescence imaging of ROS generation in HCT116L cells, including total ROS, superoxide anion, singlet oxygen, and hydroxyl radicals. (**J**) Flow cytometry analysis of ROS levels (λex = 488 nm, λem = 530 ± 30 nm, green). Error bars: S.D., $n = 3$. * $p < 0.05$, ** $p < 0.01$, *** $p < 0.001$, **** $p < 0.0001$

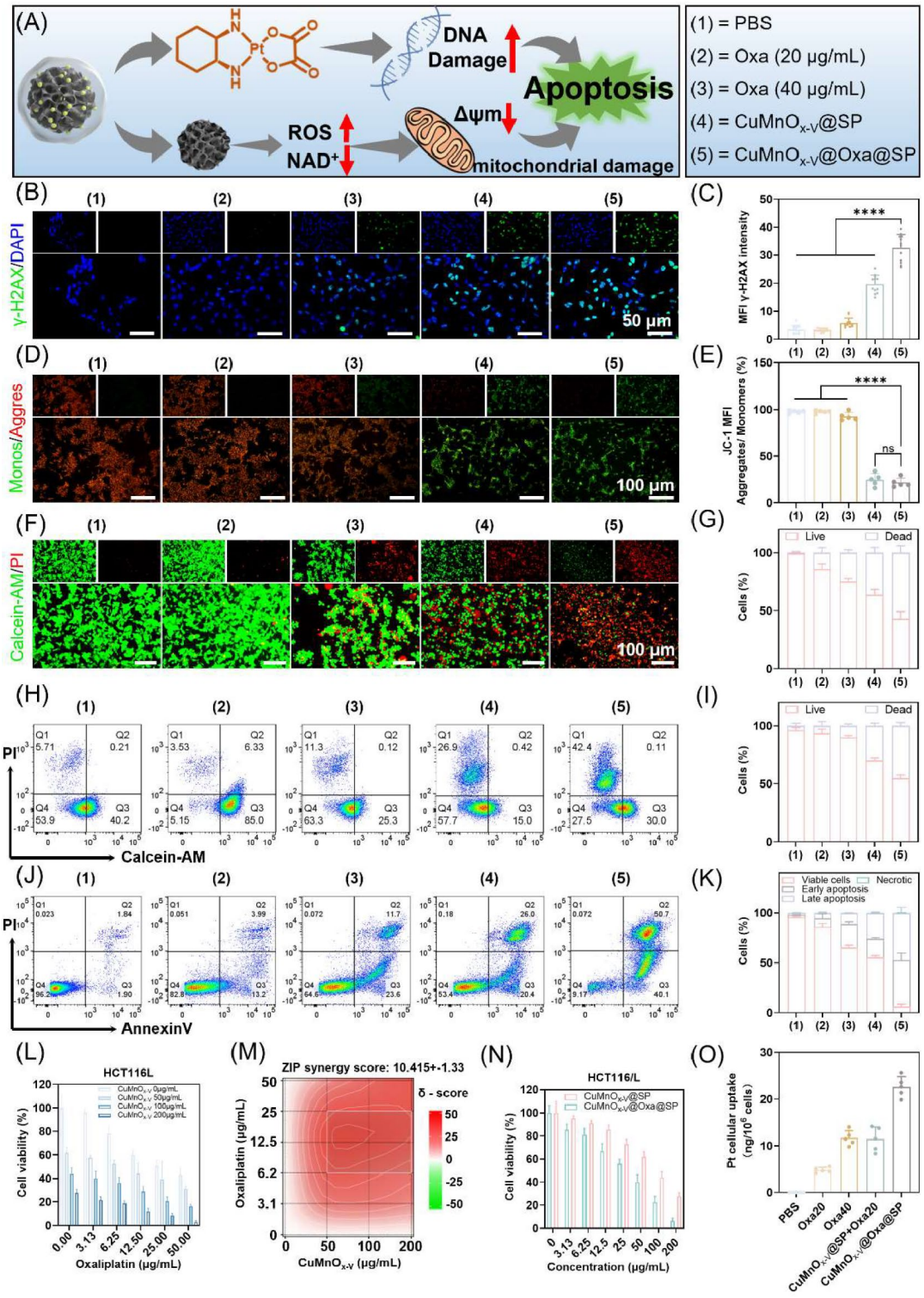

Fig. 5 Sensitization of oxaliplatin by $CuMnO_{x-V}$@Oxa@SP and evaluation of its in vitro antitumor efficacy. (**A**) Schematic illustration of the antitumor mechanism of $CuMnO_{x-V}$@Oxa@SP nanozymes. (**B**-**C**) γ-H2AX staining of HCT116/L cells under different treatments; (**D**-**E**) JC-1 staining; (**F**-**G**) Calcein-AM/PI (propidium iodide) double staining. Flow cytometry analysis of HCT116/L cell viability and death (**H**-**I**) and apoptosis (**J**-**K**). (**L**) Effect of varying concentrations of $CuMnO_{x-V}$@SP and oxaliplatin on the viability of HCT116L cells after 6 h of incubation. (**M**) Heat map of the ZIP synergy score landscape in studies combining $CuMnO_{x-V}$@SP with oxaliplatin. Red = synergistic; green = antagonistic; white = additive. A ZIP total score of 10.415 indicates strong synergy. (**N**) Effects of different concentrations of $CuMnO_{x-V}$@SP and $CuMnO_{x-V}$@Oxa@SP on HCT116/L cell viability after 6 h of treatment. (**O**) Intracellular platinum content in HCT116/L cells after 6 h of treatment, measured by ICP-MS. Groups include PBS, oxaliplatin 20 μg/mL, oxaliplatin 40 μg/mL, $CuMnO_{x-V}$@SP 100 μg/mL + oxaliplatin 20 μg/mL, and $CuMnO_{x-V}$@Oxa@SP 100 μg/mL loaded with 20 μg/mL oxaliplatin

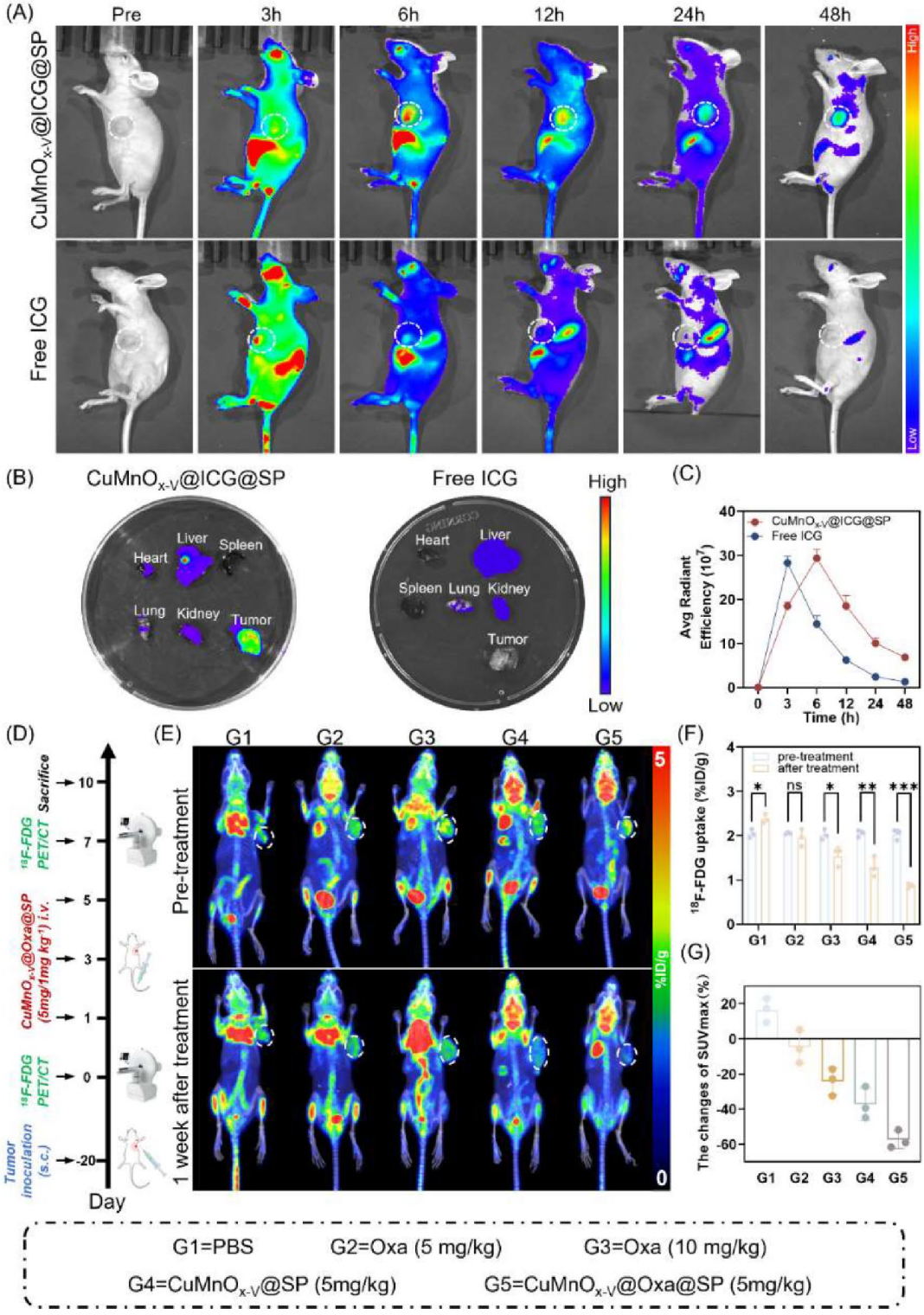

Fig. 6 In vivo fluorescence imaging with CuMnO$_{x-V}$@ICG@SP and ^{18}F-FDG PET-CT were used to assess the inhibitory effects of CuMnO$_{x-V}$@Oxa@SP on tumor glucose metabolism. (**A**) Fluorescence imaging of HCT116/L tumor-bearing mice at various time points following intravenous injection of CuMnO$_{x-V}$@ICG@SP (5 mg/1 mg/kg) and free ICG (1 mg/kg). (**B**) Ex vivo fluorescence imaging of major organs and tumors at 24 h post-injection. (**C**) Fluorescence intensity of the tumor at different time points shown in (**A**). (**D**) Schematic of the animal study design for assessing the impact of CuMnO$_{x-V}$@ICG@SP on glucose metabolism in HCT116/L tumor-bearing mice. (**E**) Representative pre- and post-treatment ^{18}F-FDG PET/CT images (tumors indicated by white circles). (**F**) and (**G**) Quantitative analysis corresponding to the data in (**E**). Error bars: S.D., $n = 3$, * $p < 0.05$, ** $p < 0.01$, *** $p < 0.001$, **** $p < 0.0001$

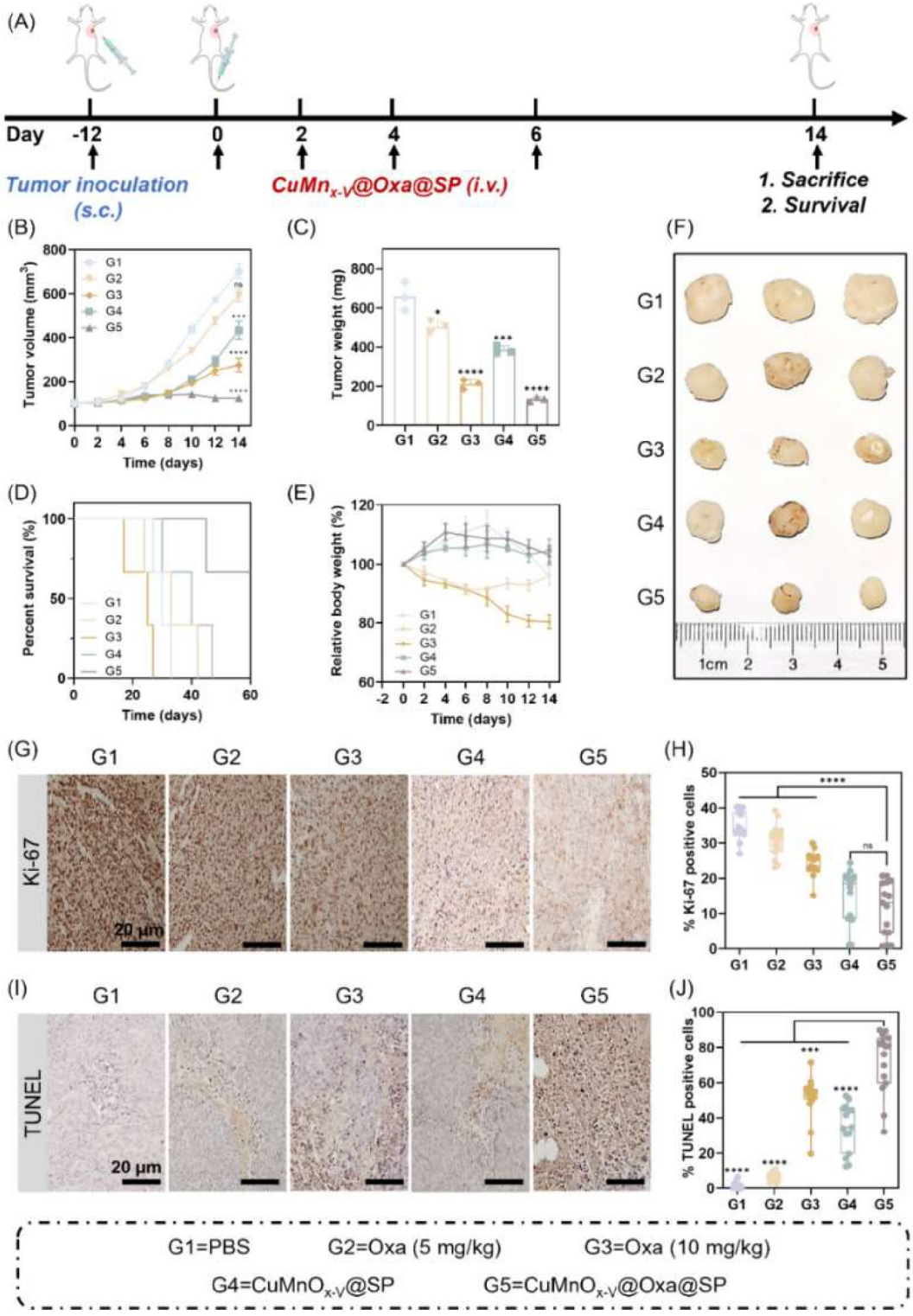

Fig. 7 In vivo therapeutic response in HCT116/L tumor-bearing mice. (**A**) Schematic of the animal experiment design. (**B**) Tumor volume measurements. (**C**) Tumor weights after 14 days of treatment with different formulations, $n = 3$. (**D**) Survival curves of treated mice, $n = 3$. (**E**) Body weight changes in tumor-bearing mice during the treatment period. (**F**) Representative images of excised tumors after 14 days of treatment. (**G**) Immunohistochemical staining for Ki-67 and (**I**) TUNEL staining. (**H**) Quantitative analysis of Ki-67 positive cells and (**J**) TUNEL positive cell proportions. Error bars: S.D., * $p < 0.05$, ** $p < 0.01$, *** $p < 0.001$, **** $p < 0.0001$

oxaliplatin resistance by disrupting NAD^+ metabolism, enhancing oxidative stress, and synergizing with oxaliplatin to inhibit tumor metabolism and growth. The combination therapy offers enhanced efficacy with reduced chemotherapy-associated toxicity, making it a promising approach for biomedical applications.

RNA sequencing (RNA-seq) transcriptome analysis

To investigate the anticancer mechanism of $CuMnO_{x-V}$@Oxa@SP, we performed RNA-Seq transcriptomic analysis of HCT116/L cells treated with $CuMnO_{x-V}$@Oxa@SP (C), oxaliplatin (O), or PBS (P) for 24 h (Fig. 8A). Both treatments significantly altered gene expression and cell signaling pathways compared to PBS (Fig. 8A, E-F). Key glycolytic enzymes such as ALDOA, ENO1, and HK1 were notably affected (Fig. 8B). Oxaliplatin treatment (OvsP) caused upregulation of glycolysis-related genes, suggesting enhanced glucose metabolism in resistance. In contrast, $CuMnO_{x-V}$@Oxa@SP treatment (CvsP, CvsO) downregulated these genes, disrupting glycolysis and glucose metabolism, consistent with ^{18}F-FDG glucose metabolism results (Fig. 4E).

Oxidative phosphorylation was also impacted (Fig. 8C). Oxaliplatin treatment upregulated components like ATP6V1F and COX6C, indicating increased energy demand to counteract DNA damage and ROS. $CuMnO_{x-V}$@Oxa@SP treatment reversed this, downregulating oxidative phosphorylation genes, consistent with ATP content measurements (Fig. 4F). These results suggest $CuMnO_{x-V}$@Oxa@SP disrupts NAD^+ metabolism and inhibits glycolysis and oxidative phosphorylation, imposing a dual blockade on HCT116/L cells' bioenergetic processes.

Oxaliplatin resistance-related genes such as AKT1, PLK1, and DKK1 were significantly downregulated upon $CuMnO_{x-V}$@Oxa@SP treatment (Fig. 8D). For example, AKT1 enhances glucose metabolism, contributing to resistance [39], while PLK1 and DKK1 promote chemotherapy resistance and poor prognosis [40, 41]. $CuMnO_{x-V}$@Oxa@SP effectively reversed the expression of these genes, overcoming oxaliplatin resistance in HCT116/L cells.

Further, GSTP1 expression, a key drug-resistance protein [42, 43], was reduced in HCT116/L cells treated with $CuMnO_{x-V}$@SP and $CuMnO_{x-V}$@Oxa@SP (Fig. 8G-H). This reduction increased intracellular oxaliplatin accumulation, highlighting the potential of nanozymes in modulating drug metabolism and overcoming resistance. $CuMnO_{x-V}$@Oxa@SP treatment also upregulated genes like BNIP2 and FOS, which enhance sensitivity to oxaliplatin [44] (Fig. 8D). These findings suggest that $CuMnO_{x-V}$@Oxa@SP sensitizes HCT116/L cells to oxaliplatin, improving its therapeutic efficacy.

Enrichment analysis of differentially expressed genes (Fig. 8E) showed enrichment in processes like cell growth, apoptosis, and DNA replication, with significant suppression of glycolysis and oxidative phosphorylation. KEGG pathway analysis (Fig. 8F) revealed positive enrichment in IL-17, NF-kB, and ferroptosis-related pathways, and negative enrichment in Rap1, Ras, and Wnt pathways, key players in colorectal cancer progression and chemoresistance [45, 46, 47]. These results underscore the dual therapeutic effects of $CuMnO_{x-V}$@Oxa@SP in disrupting energy metabolism and overcoming oxaliplatin resistance in CRC [48].

Discussion

Oxaliplatin-based chemotherapy regimens are widely used for the effective maintenance treatment of patients with advanced CRC. However, approximately 50% of patients rapidly develop resistance, and even those initially responsive eventually acquire resistance, posing significant challenges to CRC treatment [3]. This study introduces $CuMnO_{x-V}$@Oxa@SP, a novel multifunctional bimetallic nanozyme engineered with oxygen vacancies to address oxaliplatin resistance in CRC. The nanozyme exhibits multi-enzyme mimetic activities, including NAD^+ oxidase-like, OXD, and POD activities, enabling rapid and irreversible NAD^+ consumption. By disrupting the ETC and tumor antioxidant defense systems, this multifunctional nanozyme effectively exposes the metabolic vulnerabilities of chemoresistant tumor cells. Additionally, it facilitates oxaliplatin delivery, synergistically enhancing antitumor efficacy while minimizing chemotherapy-associated toxicity and improving patient outcomes.

Our findings revealed further upregulation of NAD^+ levels in oxaliplatin-resistant CRC cells (Fig. 3B-C), potentially attributed to oxaliplatin-induced NAMPT overexpression (Fig. 3D). Elevated NAD^+ levels support DNA repair, mitochondrial ETC activity, and antioxidant defenses, contributing to chemoresistance. Notably, intracellular NAD^+ directly inhibits oxaliplatin-induced apoptosis, sustaining tumor survival during chemotherapy (Fig. 3). Previous studies have explored NAD^+ targeting, such as Wang et al.'s development of a water-soluble conjugated polymer catalyst that slowly degrades NAD^+ in breast cancer cells under white light, impairing mitochondrial ETC [25]. However, the practical clinical use of this method is constrained by the challenges associated with delivering white light to deep tissues and the relatively low activity of the catalyst. Similarly, traditional NAMPT inhibitors are often associated with severe toxicity and resistance [8, 9, 10, 11]. By irreversibly degrading NAD^+ (Fig. 4C, Figure S3), thereby blocking mitochondrial ETC and tumor ADS, $CuMnO_{x-V}$@Oxa@SP uniquely circumvents these limitations, offering

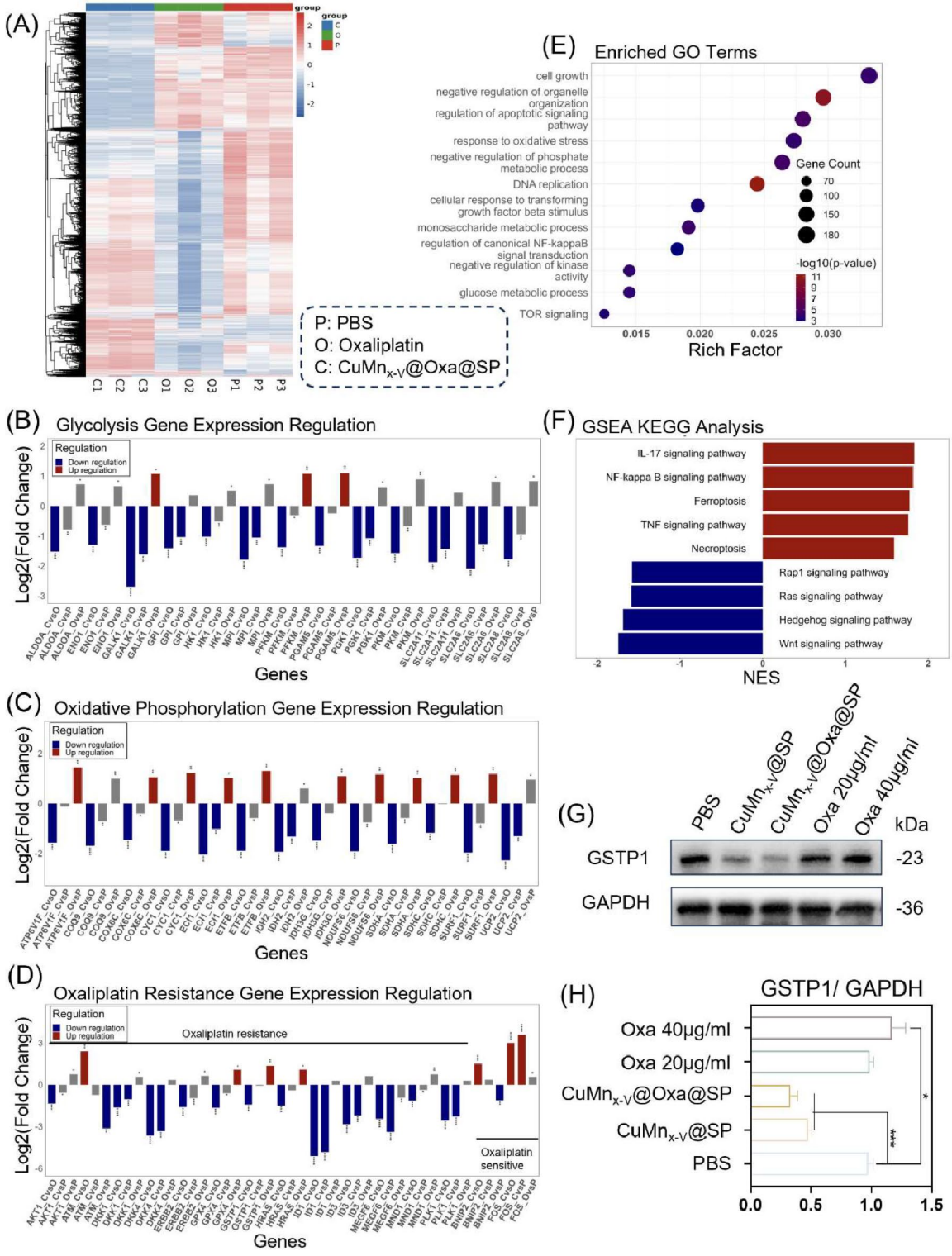

Fig. 8 RNA-Seq analysis of potential antitumor effects of CuMnO$_{x-V}$@Oxa@SP. (**A**) Heatmap of differentially expressed genes in PBS-treated and Oxaliplatin- and CuMnO$_{x-V}$@Oxa@SP-treated HCT116/L cells analyzed by RNA sequencing, (**B**-**D**) CuMnO$_{x-V}$@Oxa@SP, Oxaliplatin and PBS-treated HCT116/L cells for the regulation of glycolysis, oxidative phosphorylation and oxaliplatin resistance-related gene expression. (**E**) GO enrichment analysis to identify the pathways mediated by CuMnO$_{x-V}$@Oxa@SP treatment compared to Oxaliplatin-treated group. (**F**) KEGG enrichment analysis identifying pathways mediated after CuMnO$_{x-V}$@Oxa@SP treatment compared to Oxaliplatin-treated group. (**G**-**H**) Immunoblotting and normalized grayscale values of GSTP1 in HCT116/L cells after treatment with different formulations for 24 H. $n = 3$, Error bars: S.D., * $p < 0.05$, ** $p < 0.01$, *** $p < 0.001$, **** $p < 0.0001$

a novel therapeutic strategy to overcome clinical oxaliplatin resistance.

Compared to monometallic nanozymes, bimetallic nanozymes have demonstrated superior catalytic activity and stability due to their multi-catalytic active sites, making them widely applicable in cancer research [22]. In this study, copper ions were combined with manganese ions, leveraging the strong substrate adsorption capabilities of copper sites to lower energy barriers for intermediate products while enhancing catalytic activity through electron interactions with neighboring atoms. The addition of manganese ions introduced multi-enzyme mimetic activities and TME-responsive degradability, mitigating the long-term toxicity of copper ions. In the field of cancer therapy, bimetallic nanozymes show great application potential. They can generate ROS and belong to oxygen-dependent therapy. However, the hypoxic microenvironment of solid tumors greatly reduces the efficacy of oxygen-dependent therapy [49]. Meanwhile, intracellular overexpression of NAD^+ significantly decreases cellular ROS levels, enhancing NAD^+-related antioxidant defense systems and further limiting the therapeutic effect of oxygen-dependent therapy. In this study, we innovatively introduced a NAD^+-targeting consumption therapeutic strategy to disrupt the antioxidant defense barriers of tumor cells and increase their sensitivity to ROS. Our results demonstrated that $CuMnO_{x-V}$@Oxa@SP generates a ROS storm (Fig. 2 and 4), amplifying oxidative stress in tumor cells. This mechanism disrupts redox balance and mitochondrial function, triggering apoptosis in oxaliplatin-resistant cells. Importantly, this nanozyme's NAD^+ catalytic decomposition is oxygen-independent (Figure S3), allowing it to effectively consume NAD^+ in hypoxic environments. This enhances the sensitivity of oxygen-dependent therapy, overcomes its limitations, and broadens its application prospects in solid tumor treatment.

Good biocompatibility is essential for nanomaterials in biomedical applications [50]. Our results show that nanozyme-loaded oxaliplatin, with pH-responsive release (Fig. 1Q), reduces liver/kidney damage and cardiotoxicity compared to free oxaliplatin (Figure S14-16). After 14 days of treatment, vital organ slices from the nanodrug group show no significant damage, indicating good in vivo safety and tolerability. Biodistribution analysis reveals nanozymes mainly accumulate in the liver, spleen, and tumor, favoring hepatobiliary excretion and reducing accumulation risk, thus enhancing clinical application safety. Previous studies have shown that GSTP1 binds reduced glutathione (GSH) to platinum compounds, forming soluble, non-toxic GS-Pt derivatives that are easily excreted [51]. Our study demonstrated that $CuMnO_{x-V}$@Oxa@SP downregulates GSTP1 expression (Fig. 8G-H), increasing intracellular drug retention (Fig. 5O) and restoring chemosensitivity. The dual inhibition of GSTP1 and NAD^+ consumption impairs tumor defenses against DNA damage and oxidative stress.

Moreover, dual targeting of energy metabolism and ROS defenses represents an effective strategy to overcome CRC chemoresistance. Our findings indicate that $CuMnO_{x-V}$@Oxa@SP significantly reduces glucose metabolism and ATP production in HCT116/L cells (Fig. 4E-F), consistent with results from oxaliplatin-resistant CRC mouse models (Fig. 6E-G). Furthermore, $CuMnO_{x-V}$@Oxa@SP effectively induces DNA damage, disrupts ETC, and promotes apoptosis in vitro (Fig. 5) while inhibiting tumor growth in vivo (Fig. 7B). Ki-67 staining confirmed reduced cell proliferation (Fig. 7G), and the presence of large necrotic regions and apoptotic cells in TUNEL staining (Fig. 7I) corroborated these findings, despite no significant reduction in tumor volume.

Although $CuMnO_{x-V}$@Oxa@SP shows great therapeutic potential, several limitations require further investigation. For instance, this study employed a subcutaneous xenograft model using nude mice due to the challenges of constructing oxaliplatin-resistant orthotopic CRC models. Consequently, the immune activation potential of the nanozyme remains unexplored. Future studies should address these issues to further validate the therapeutic efficacy of $CuMnO_{x-V}$@Oxa@SP. Secondly, in the design of nanozymes, bioinformatics analysis can be used to find more effective catalytic targets [52], thereby enhancing the effectiveness and targeting of nanozymes.

Conclusion

In summary, to address therapy resistance caused by excessive NAD^+ accumulation due to tumor NAMPT hyperactivation, we rationally designed and developed a novel multifunctional oxygen-vacancy-engineered bimetallic nanozyme. This nanozyme exhibits remarkable NAD^+-mimicking activity, enabling the rapid, sustained, and irreversible degradation of NAD^+ and its derived cofactors while blocking the NAD synthesis salvage pathway. The irreversible breakdown of NAD^+ suppresses DNA repair mechanisms, disrupts the ETC, damages mitochondria, and cuts off the energy supply, thereby exposing the metabolic vulnerabilities of tumor cells. Moreover, the nanozyme demonstrates POD- and OXD-like activities and leverages the Fenton-like activity of Cu^{2+} and Mn^{2+} to induce an intracellular ROS surge, triggering apoptosis pathways. It also inhibits GSTP1 expression, thereby blocking the GSTP1-dependent oxaliplatin detoxification pathway, enhancing oxaliplatin efficacy, and reducing chemotherapy side effects while exploiting its weaknesses. Consequently, $CuMnO_{x-V}$@Oxa@SP NFs exhibit significant therapeutic efficacy in an oxaliplatin-resistant colorectal cancer model. This work not only advances the design of defect-engineered nanozymes and

unlocks the potential of nanozyme-mediated metabolic intervention in cancer therapy but also offers a novel strategy and therapeutic approach for clinically challenging tumors.

Supplementary Information

The online version contains supplementary material available at https://doi.org/10.1186/s12951-025-03417-8.

Supplementary Material 1

Author contributions

Investigation: DZ, XXY, JHY and ZSL. Analysis: DZ, XXY and YJL. Bioinformatics: MTM. Design and Supervision: DZ, XXY, JL and SH. Funding acquisition: SH, JL and XXY. Manuscript Preparation (original draft and review): DZ, XXY, ZCF, YXT and YW. All authors reviewed and approved the final manuscript.

Funding

This work was supported by the National Natural Science Foundation of China (No. 82272045), (U22A20303), Postdoctoral Fellowship Program of CPSF under Grant Number GZC20233197, China Postdoctoral Science Foundation under Grant Number 2024M753675, Science and Technology Innovation Program of Hunan Province (2021RC4056), (2021RC4016), Clinical Research Center for Medical Imaging in Hunan Province (2020SK400), and Key Program of Ministry of Industry and Information Technology of China (CEIEC-2022-ZM02-0219).

Data availability

No datasets were generated or analysed during the current study.

Declarations

Ethics approval and consent to participate

All animal experiments were approved by the Institutional Animal Care and Use Committee (IACUC) (Certificate No. 20220533) following the Guidelines for the Care and Use of Laboratory.

Consent for publication

All authors have consented to submit this article for publication.

Competing interests

The authors declare no competing interests.

Author details

[1]Department of Nuclear Medicine, Xiangya Hospital, Central South University, 87 Xiangya Road, Changsha, Hunan 410008, China
[2]Department of Radiology, Second Xiangya Hospital of Central South University, 139 Renming Middle Road Changsha, Changsha, Hunan, China
[3]SJTU-Ruijin-UIH Institute for Medical Imaging Technology Ruijin Hospital, Shanghai Jiao Tong University School of Medicine, Shanghai, China
[4]Department of Radiology, The First Hospital of Hunan University of Chinese Medicine, Changsha, Hunan, China
[5]Department of Radiology, The Third Xiangya Hospital, Central South University, Changsha, Hunan, China
[6]Furong Laboratory, Central South University, Changsha, Hunan 410008, China
[7]National Clinical Research Center for Geriatric Disorders (XIANGYA), Xiangya Hospital, Central South University, Changsha, Hunan, China
[8]Key Laboratory of Biological Nanotechnology of National Health Commission, Xiangya Hospital, Central South University, Changsha, Hunan, China

Received: 24 January 2025 / Accepted: 26 April 2025
Published online: 16 May 2025

References

1. Siegel RL, Miller KD, Wagle NS, Jemal A. Cancer statistics, 2023. CA Cancer J Clin. 2023;73:17–48.
2. Woolf SH. The best screening test for colorectal cancer–a personal choice. N Engl J Med. 2000;343:1641–3.
3. Li Y, Gan Y, Liu J, Li J, Zhou Z, Tian R, Sun R, Liu J, Xiao Q, Li Y, et al. Downregulation of MEIS1 mediated by ELFN1-AS1/EZH2/DNMT3a axis promotes tumorigenesis and oxaliplatin resistance in colorectal cancer. Signal Transduct Target Ther. 2022;7:87.
4. Hong SM, Hwang SW, Wang T, Park CW, Ryu YM, Jung JH, Shin JH, Kim SY, Lee JL, Kim CW, et al. Increased nicotinamide adenine dinucleotide pool promotes colon cancer progression by suppressing reactive oxygen species level. Cancer Sci. 2019;110:629–38.
5. Lucena-Cacace A, Otero-Albiol D, Jimenez-Garcia MP, Munoz-Galvan S, Carnero A. NAMPT is a potent oncogene in Colon Cancer progression that modulates Cancer stem cell properties and resistance to therapy through Sirt1 and PARP. Clin Cancer Res. 2018;24:1202–15.
6. Lin JF, Hu PS, Wang YY, Tan YT, Yu K, Liao K, Wu QN, Li T, Meng Q, Lin JZ, et al. Phosphorylated NFS1 weakens oxaliplatin-based chemosensitivity of colorectal cancer by preventing PANoptosis. Signal Transduct Target Ther. 2022;7:54.
7. Sampath D, Zabka TS, Misner DL, O'Brien T, Dragovich PS. Inhibition of nicotinamide phosphoribosyltransferase (NAMPT) as a therapeutic strategy in cancer. Pharmacol Ther. 2015;151:16–31.
8. Nacarelli T, Fukumoto T, Zundell JA, Fatkhutdinov N, Jean S, Cadungog MG, Borowsky ME, Zhang R. NAMPT Inhibition suppresses Cancer Stem-like cells associated with Therapy-Induced senescence in ovarian Cancer. Cancer Res. 2020;80:890–900.
9. Yong J, Cai S, Zeng Z. Targeting NAD(+) metabolism: dual roles in cancer treatment. Front Immunol. 2023;14:1269896.
10. von Heideman A, Berglund A, Larsson R, Nygren P. Safety and efficacy of NAD depleting cancer drugs: results of a phase I clinical trial of CHS 828 and overview of published data. Cancer Chemother Pharmacol. 2010;65:1165–72.
11. Gordeuk VR, Campbell A, Rana S, Nouraie M, Niu X, Minniti CP, Sable C, Darbari D, Dham N, Onyekwere O, et al. Relationship of erythropoietin, fetal hemoglobin, and hydroxyurea treatment to tricuspid regurgitation velocity in children with sickle cell disease. Blood. 2009;114:4639–44.
12. Wang H, Wan K, Shi X. Recent advances in nanozyme research. Adv Mater. 2019;31:e1805368.
13. Liu J, Yu B, Rong M, Sun W, Lu L. A new strategy to fight tumor heterogeneity: integrating metal-defect active centers within NADH oxidase nanozymes. Nano Today 2024:54.
14. Ge M, Zhu W, Mei J, Hu T, Yang C, Lin H, Shi J. Piezoelectric-Enhanced nanocatalysts trigger neutrophil N1 polarization against bacterial biofilm by disrupting redox homeostasis. Adv Mater 2024:e2409633.
15. Liang K, Nan F, Wang J, Zhang Y, Li J, Xue X, Chen T, Hao Y, Wang P, Ge J. A versatile Nanozyme-Based NADH Circulating oxidation reactor for tumor therapy through triple cellular metabolism disruption. Small. 2024;20:e2311027.
16. Navas LE, Carnero A. NAD(+) metabolism, stemness, the immune response, and cancer. Signal Transduct Target Ther. 2021;6:2.
17. Vitale I, Shema E, Loi S, Galluzzi L. Intratumoral heterogeneity in cancer progression and response to immunotherapy. Nat Med. 2021;27:212–24.
18. Wang Z, Wu B, Nie G, Wei J, Li Y. Regulation of metabolism in pancreatic ductal adenocarcinoma via nanotechnology-enabled strategies. Cancer Lett. 2023;560:216138.
19. Liu Q, Zhang A, Wang R, Zhang Q, Cui D. A review on metal- and metal Oxide-Based nanozymes: properties, mechanisms, and applications. Nanomicro Lett. 2021;13:154.
20. Liu Y, Zhao H, Zhao Y. Designing efficient single metal atom biocatalysts at the atomic structure level. Angew Chem Int Ed Engl. 2024;63:e202315933.
21. Liang X, Fu N, Yao S, Li Z, Li Y. The progress and outlook of metal Single-Atom-Site catalysis. J Am Chem Soc. 2022;144:18155–74.
22. Tompkins FC. Superficial chemistry and solid imperfections. Nature. 1960;186:3–6.
23. Gao Y, Liu S, Liu H, Ge H, Zhang M, Zhao C, Gong Y, Zhang X, Wang C, Sun X. Application of oxygen vacancy defects in enhanced anti-cancer nanomedicine. Sci China Chem. 2023;66:2492–512.
24. Ren Z, Ruan L, Yin L, Akkiraju K, Giordano L, Liu Z, Li S, Ye Z, Li S, Yang H, et al. Surface oxygen vacancies confined by ferroelectric polarization for tunable CO oxidation kinetics. Adv Mater. 2022;34:e2202072.
25. Xia S, Bai H, Zhang E, Yu W, Gao Z, Lv F, Huang Y, Zhu D, Wang S. Unexpected photocatalytic degeneration of NAD < sup>+ for inducing apoptosis of hypoxia Cancer cells. CCS Chem. 2023;5:2324–33.

26. Solier S, Muller S, Caneque T, Versini A, Mansart A, Sindikubwabo F, Baron L, Emam L, Gestraud P, Pantos GD, et al. A druggable copper-signalling pathway that drives inflammation. Nature. 2023;617:386–94.
27. Sun Z, Li C, Wei Z, Zhang F, Deng Z, Zhou K, Wang Y, Guo J, Yang J, Xiang Z, et al. Sulfur-Bridged asymmetric CuNi bimetallic atom sites for CO(2) reduction with high efficiency. Adv Mater. 2024;36:e2404665.
28. Jiao L, Tao N, Kang YK, Song WY, Chen YF, Zhang Y, Xu WQ, Wu Y, Gu WL, Zheng LR et al. Biomimetic Fe-Cu Dual-atomic-site catalysts enable efficient H2O2 activation for tumor lymphatic metastasis Inhibition. Nano Today 2023, 50.
29. Ding B, Zheng P, Jiang F, Zhao Y, Wang M, Chang M, Ma P, Lin J. MnO(x) nanospikes as nanoadjuvants and Immunogenic cell death drugs with enhanced antitumor immunity and antimetastatic effect. Angew Chem Int Ed Engl. 2020;59:16381–4.
30. Liu Z, Zhao M, Lin H, Dai C, Ren C, Zhang S, Peng W, Chen Y. 2D magnetic titanium carbide MXene for cancer theranostics. J Mater Chem B. 2018;6:3541–8.
31. Gu X, Yue J, Li L, Xue H, Yang J, Zhao X. General synthesis of MnOx (MnO2, Mn2O3, Mn3O4, MnO) hierarchical microspheres as Lithium-ion battery anodes. Electrochim Acta. 2015;184:250–6.
32. Kong J, Ma S, Chu R, Liu J, Yu H, Mao M, Ge X, Sun Y, Wang Y. Photothermal and photocatalytic glycol Chitosan and Polydopamine-Grafted oxygen vacancy bismuth Oxyiodide (BiO(1-x) I) nanoparticles for the diagnosis and targeted therapy of diabetic wounds. Adv Mater. 2024;36:e2307695.
33. Zhang S, Shi J, Chen Y, Huo Q, Li W, Wu Y, Sun Y, Zhang Y, Wang X, Jiang Z. Unraveling and manipulating of NADH oxidation by photogenerated holes. ACS Catal. 2020;10:4967–72.
34. Amaravadi RK, Kimmelman AC, Debnath J. Targeting autophagy in cancer: recent advances and future directions. Cancer Discov. 2019;9:1167–81.
35. Ou J, Peng Y, Yang W, Zhang Y, Hao J, Li F, Chen Y, Zhao Y, Xie X, Wu S, et al. ABHD5 blunts the sensitivity of colorectal cancer to fluorouracil via promoting autophagic uracil yield. Nat Commun. 2019;10:1078.
36. Luengo A, Li Z, Gui DY, Sullivan LB, Zagorulya M, Do BT, Ferreira R, Naamati A, Ali A, Lewis CA, et al. Increased demand for NAD(+) relative to ATP drives aerobic Glycolysis. Mol Cell. 2021;81:691–e707696.
37. Chen HY, Islam A, Yuan TM, Chen SW, Liu PF, Chueh PJ. Regulation of tNOX expression through the ROS-p53-POU3F2 axis contributes to cellular responses against oxaliplatin in human colon cancer cells. J Exp Clin Cancer Res. 2018;37:161.
38. Rahman AA, Masango P, Stavely R, Bertrand P, Page A, Nurgali K. Oxaliplatin-Induced damage to the gastric innervation: role in nausea and vomiting. Biomolecules 2023, 13.
39. Park GB, Jeong JY, Kim D. GLUT5 regulation by AKT1/3-miR-125b-5p down-regulation induces migratory activity and drug resistance in TLR-modified colorectal cancer cells. Carcinogenesis. 2020;41:1329–40.
40. Abumustafa W, Castven D, Becker D, Salih SS, Manzoor S, Zamer BA, Talaat I, Hamad M, Marquardt JU, Muhammad JS. Inhibition of PRMT5-mediated regulation of DKK1 sensitizes colorectal cancer cells to chemotherapy. Cell Signal. 2024;119:111166.
41. He S, Shen J, Hu N, Xu X, Li J. DKK4 enhances resistance to chemotherapeutics 5-Fu and YN968D1 in colorectal cancer cells. Oncol Lett. 2017;13:587–92.
42. Ghanbarian M, Afgar A, Yadegarazari R, Najafi R, Teimoori-Toolabi L. Through oxaliplatin resistance induction in colorectal cancer cells, increasing ABCB1 level accompanies decreasing level of miR-302c-5p, miR-3664-5p and miR-129-5p. Biomed Pharmacother. 2018;108:1070–80.
43. Fang Y, Ye J, Zhao B, Sun J, Gu N, Chen X, Ren L, Chen J, Cai X, Zhang W, et al. Formononetin ameliorates oxaliplatin-induced peripheral neuropathy via the KEAP1-NRF2-GSTP1 axis. Redox Biol. 2020;36:101677.
44. He Y, Ling Y, Zhang Z, Mertens RT, Cao Q, Xu X, Guo K, Shi Q, Zhang X, Huo L, et al. Butyrate reverses ferroptosis resistance in colorectal cancer by inducing c-Fos-dependent xCT suppression. Redox Biol. 2023;65:102822.
45. Ma Y, Aymeric L, Locher C, Mattarollo SR, Delahaye NF, Pereira P, Boucontet L, Apetoh L, Ghiringhelli F, Casares N, et al. Contribution of IL-17-producing gamma delta T cells to the efficacy of anticancer chemotherapy. J Exp Med. 2011;208:491–503.
46. Zhou Y, Bastian IN, Long MD, Dow M, Li W, Liu T, Ngu RK, Antonucci L, Huang JY, Phung QT et al. Activation of NF-kappaB and p300/CBP potentiates cancer chemoimmunotherapy through induction of MHC-I antigen presentation. Proc Natl Acad Sci U S A 2021, 118.
47. Zhu G, Pei L, Xia H, Tang Q, Bi F. Role of oncogenic KRAS in the prognosis, diagnosis and treatment of colorectal cancer. Mol Cancer. 2021;20:143.
48. Liu X, Su K, Sun X, Jiang Y, Wang L, Hu C, Zhang C, Lu M, Du X, Xing B. Section 62 promotes stemness and chemoresistance of human colorectal cancer through activating Wnt/beta-catenin pathway. J Exp Clin Cancer Res. 2021;40:132.
49. Chen Y, Deng Y, Li Y, Qin Y, Zhou Z, Yang H, Sun Y. Oxygen-Independent radiodynamic therapy: Radiation-Boosted chemodynamics for reprogramming the tumor immune environment and enhancing antitumor immune response. ACS Appl Mater Interfaces. 2024;16:21546–56.
50. Jiang Z, Li Y, Wei Z, Yuan B, Wang Y, Akakuru OU, Li Y, Li J, Wu A. Pressure-induced amorphous zeolitic imidazole frameworks with reduced toxicity and increased tumor accumulation improves therapeutic efficacy in vivo. Bioact Mater. 2021;6:740–8.
51. Schnekenburger M, Karius T, Diederich M. Regulation of epigenetic traits of the glutathione S-transferase P1 gene: from detoxification toward cancer prevention and diagnosis. Front Pharmacol. 2014;5:170.
52. Su Y, Tian X, Gao R, Guo W, Chen C, Chen C, Jia D, Li H, Lv X. Colon cancer diagnosis and staging classification based on machine learning and bioinformatics analysis. Comput Biol Med. 2022;145:105409.

Publisher's note

Springer Nature remains neutral with regard to jurisdictional claims in published maps and institutional affiliations.